ARL-TR-9138 • JAN 2021

DEVCOM ARMY RESEARCH LABORATORY

A Continuum Model of the Human Lung: Implementation and Parameterization

by John D Clayton, Rohan J Banton, and Alan R Goertz

Approved for public release; distribution is unlimited.

NOTICES

Disclaimers

The findings in this report are not to be construed as an official Department of the Army position unless so designated by other authorized documents.

Citation of manufacturer's or trade names does not constitute an official endorsement or approval of the use thereof.

Destroy this report when it is no longer needed. Do not return it to the originator.

ARL-TR-9138 ● JAN 2021



A Continuum Model of the Human Lung: Implementation and Parameterization

John D Clayton and Rohan J Banton
Weapons and Materials Research Directorate, DEVCOM Army Research Laboratory

Alan R Goertz
SURVICE Engineering Company

Approved for public release; distribution is unlimited.

REPORT DOCUMENTATION PAGE

Form Approved
OMB No. 0704-0188

Public reporting burden for this collection of information is estimated to average 1 hour per response, including the time for reviewing instructions, searching existing data sources, gathering and maintaining the data needed, and completing and reviewing the collection information. Send comments regarding this burden estimate or any other aspect of this collection of information, including suggestions for reducing the burden, to Department of Defense, Washington Headquarters Services, Directorate for Information Operations and Reports (0704-0188), 1215 Jefferson Davis Highway, Suite 1204, Arlington, VA 22202-4302. Respondents should be aware that notwithstanding any other provision of law, no person shall be subject to any penalty for failing to comply with a collection of information if it does not display a currently valid OMB control number.

PLEASE DO NOT RETURN YOUR FORM TO THE ABOVE ADDRESS.

1. REPORT DATE *(DD-MM-YYYY)*	2. REPORT TYPE	3. DATES COVERED (From - To)
January 2021	Technical Report	June 2020–January 2021

4. TITLE AND SUBTITLE
A Continuum Model of the Human Lung: Implementation and Parameterization

5a. CONTRACT NUMBER

5b. GRANT NUMBER

5c. PROGRAM ELEMENT NUMBER

6. AUTHOR(S)
John D Clayton, Rohan J Banton, and Alan R Goertz

5d. PROJECT NUMBER

5e. TASK NUMBER

5f. WORK UNIT NUMBER

7. PERFORMING ORGANIZATION NAME(S) AND ADDRESS(ES)
DEVCOM Army Research Laboratory
ATTN: FCDD-RLW-PC
Aberdeen Proving Ground, MD 21005-5066

8. PERFORMING ORGANIZATION REPORT NUMBER
ARL-TR-9138

9. SPONSORING/MONITORING AGENCY NAME(S) AND ADDRESS(ES)

10. SPONSOR/MONITOR'S ACRONYM(S)

11. SPONSOR/MONITOR'S REPORT NUMBER(S)

12. DISTRIBUTION/AVAILABILITY STATEMENT
Approved for public release; distribution is unlimited.

13. SUPPLEMENTARY NOTES
primary author's email: <john.d.clayton1.civ@mail.mil>.

14. ABSTRACT
A continuum model for lung parenchyma is refined and implemented for numerical simulations of dynamic impact or blast loading to the human torso. Elastic stiffness parameters for the model, originally derived from experimental data for other mammals, are adapted for the human lung. Ranges of uncertain properties, specifically those describing initial mass density and damage kinetics, are investigated in numerical studies. Algorithms for computer implementation as a user material subroutine in the LS-DYNA software are described. Simulations of the human torso impacted by a rod at velocities up to 90 m/s are reported. Predictions of severity of local trauma to the lung tissue are analyzed, and global injury metrics are examined.

15. SUBJECT TERMS
nonlinear elasticity, viscoelasticity, damage mechanics, injury mechanisms, soft solids, lung, shock waves

16. SECURITY CLASSIFICATION OF:			17. LIMITATION OF ABSTRACT	18. NUMBER OF PAGES	19a. NAME OF RESPONSIBLE PERSON
a. REPORT	b. ABSTRACT	c. THIS PAGE			John D Clayton
Unclassified	Unclassified	Unclassified	UU	81	19b. TELEPHONE NUMBER (Include area code) 410-278-6146

Standard Form 298 (Rev. 8/98)
Prescribed by ANSI Std. Z39.18

Contents

List of Figures v

List of Tables vi

Acknowledgments vii

1. Introduction 1

2. Constitutive Model 3

2.1 Kinematics of Finite Deformation 4

2.2 Stress Power, Conservation Laws, and Entropy Production 7

2.3 Generic Constitutive Laws 8

2.4 Internal Energy Formulation for Air-Tissue Response 11

2.5 Viscoelasticity 17

2.6 Damage 19

2.7 Stresses, Entropy, and Temperature 23

2.8 Energy Gradient to Rate Transformation 25

2.9 Fully Intact Stiffness Model 27

3. Numerical Implementation 28

4. Parameters for the Human Lung 32

4.1 Simple Shear 33

4.2 Uniaxial Strain Compression 35

5. Human Torso Simulations 38

5.1 Advanced Total Body Model for LS–DYNA and Problem Setup 38

5.2 Results and Analysis 41

6. Conclusions 58

7. References 60

Appendix. Input File Syntax for LS–DYNA 68

Distribution List **72**

List of Figures

Fig. 1 Physical processes related to injury and microstructure degradation occurring in lung tissue in conjunction with evolution of damage state variable D. Exponential growth versus driving force is consistent with kinetic law in Eq. 76. 23

Fig. 2 Model response in dynamic simple shear at $\dot{\gamma} = 1000$ s^{-1} compared to experimental data on porcine lung[36] tested at $\dot{\gamma} = 550$ s^{-1} and human lung[43] tested at $\dot{\gamma} = 1305$ s^{-1} and $\dot{\gamma} = 2300$ s^{-1}: a) shear stress τ versus simple shear strain γ for $\omega_D = 0.5$, b) shear stress τ versus simple shear strain γ for $\omega_D = 30$, and c) damage variable D versus shear γ 34

Fig. 3 Model response for animal lung under adiabatic uniaxial strain compression at $\dot{\varepsilon} = 1000$ s^{-1}: a) longitudinal compressive stress P, b) shear stress τ, and c) damage variable D 36

Fig. 4 Model response for human lung under adiabatic uniaxial strain compression at $\dot{\varepsilon} = 1000$ s^{-1}: a) axial compressive stress P, b) shear stress τ, and c) damage variable D 37

Fig. 5 Human ATBM 2.5: a) entire model including projectile, b) skull and torso with skin and flesh removed for visualization, c) torso with skin, flesh, and skeletal system removed for visualization, and d) lungs with hexahedral mesh 39

Fig. 6 Surface displacement magnitude u, simulation 3 ($v_I = 45$ m/s): a) $t = 2$ ms, b) $t = 5$ ms, c) $t = 10$ ms, and d) $t = 30$ ms 42

Fig. 7 Surface displacement magnitude u, simulation 7 ($v_I = 90$ m/s): a) $t = 2$ ms, b) $t = 5$ ms, c) $t = 10$ ms, and d) $t = 30$ ms 43

Fig. 8 Lung damage-injury variable D, simulation 1 ($v_I = 45$ m/s, $\omega_D = 0.5$): a) $t = 2$ ms, b) $t = 5$ ms, c) $t = 10$ ms, and d) $t = 30$ ms 46

Fig. 9 Lung damage-injury variable D, simulation 3 ($v_I = 45$ m/s, $\omega_D = 30$): a) $t = 2$ ms, b) $t = 5$ ms, c) $t = 10$ ms, and d) $t = 39$ ms 47

Fig. 10 Lung damage-injury variable D, simulation 5 ($v_I = 90$ m/s, $\omega_D = 0.5$): a) $t = 2$ ms, b) $t = 5$ ms, c) $t = 10$ ms, and d) $t = 30$ ms 48

Fig. 11 Lung damage-injury variable D, simulation 7 ($v_I = 90$ m/s, $\omega_D = 30$): a) $t = 2$ ms, b) $t = 5$ ms, c) $t = 10$ ms, and d) $t = 30$ ms 49

Fig. 12 Lung damage-injury variable D at $t = 5$ ms, $v_I = 45$ m/s: a) simulation 1, b) simulation 2, c) simulation 3, and d) simulation 4 50

Fig. 13 Lung damage-injury variable D at $t = 5$ ms, $v_I = 90$ m/s: a) simulation 5, b) simulation 6, c) simulation 7, and d) simulation 8 51

Fig. 14 Lung damage-injury variable D at $t = 5$ ms, $\omega_D = 30$, and $v_I = 90$ m/s: a) simulation 7, b) simulation 8, c) simulation 9, and d) simulation 10 . 52

Fig. 15 Average damage-injury metric D_V (both lungs) versus simulation time: a) simulations 1, 2, 5, 6 ($\omega_D = 0.5$), b) simulations 3, 4, 7, 8 ($\omega_D = 30$), and c) simulations 7–10 (different stiffness options, impact velocity 90 m/s) 54

Fig. 16 Compression injury criterion C versus simulation time: a) simulations 1–4 (impact velocity 45 m/s) and b) simulations 5–8 (impact velocity 90 m/s) 55

Fig. 17 Viscous injury criterion VC versus simulation time: a) simulations 1–4 (impact velocity 45 m/s) and b) simulations 5–8 (impact velocity 90 m/s) 56

List of Tables

Table 1 Suggested parameter values for animal[18,20] and human lung parenchyma 33

Table 2 Parameters varied among `LS-DYNA` simulations of impact to the human torso 41

Table 3 Likelihood of lung injury in porcine experiments[45] compared with maximum volume-averaged damage-injury parameter $\bar{D}_{V|max}$ from `LS-DYNA` simulations of impact of the human torso. Global injury metric $\bar{D}_V$ is mean among simulations with two different lung densities ρ_0 but the same gradient amplification factor ω_D; maximum value at $t = 30$ ms shown. Also compared are two other global thoracic injury criteria[46,47]: normalized compression criteria $\bar{C}_{max}$ and viscous criteria $\overline{VC}_{max}$, where mean values over simulations with different lung densities are calculated in the same manner. 57

Acknowledgments

The authors acknowledge support of the US Army Combat Capabilities Development (DEVCOM) Army Research Laboratory (ARL). Information exchanges with Alan Freed of Texas A&M University, Richard Regueiro of the University of Colorado, Oren Petel of Carleton University, and Tim Baumer, Michael Kleinberger, and Karin Rafaels of the DEVCOM Army Research Laboratory on soft tissue biomechanics and ballistic injury mechanisms are acknowledged. The authors also acknowledge Southwest Research Institute and Elemance, LLC, with funding from the Office of Naval Research, for supplying the `LS-DYNA` input files to the Advanced Total Body Model Version 2.5 (ATBM 2.5) of the human torso and head.

1. Introduction

The lung is the largest vital organ in the human thorax by volume. Lung injuries most often arise in military operations via either dynamic blunt loading or blast loading. For blunt trauma, pulmonary contusion (i.e., severe bruising of the lung tissue) is the most common thoracic soft tissue injury. The mortality rate of such injury is 10%–25%.[1] For blast, severe damage to the lungs is the main cause of morbidity and mortality following high-level exposure.[2] Lung laceration is also commonplace in dynamic torso injuries[3]; often, fractured ribs and lung collapse are parallel contributing factors to compromised human performance.

Constitutive models of soft tissues, including those comprising the lungs, are needed for analysis and computer simulations of the human torso subjected to mechanical insult. Predictive models will enable the development of innovative protection systems for commercial and military vehicles and for Soldiers in military operations.[4]

Recent works by the authors[5,6] sought to develop such a predictive continuum mechanical constitutive model for the lung. This model describes large deformation, stress wave propagation, damage, and injury mechanisms sustained in the lung tissue when the thorax is subjected to traumatic insult by dynamic blunt impact[7–9] or rapidly rising high-pressure (i.e., blast) waves.[4,10–13] The model is more general than others known to the authors that tend to focus on a single regime (e.g., models designed exclusively for static extension, cyclic expansion as in respiration, blunt impact, or blast). It is the first known model for lung tissue mechanics that incorporates an evolving thermodynamic state variable indicative of damage,[14,15] though different kinds of damage mechanics formulations have been used for other fibrous soft biological tissues.[16,17] Notably, the load history-dependent damage variable, denoted by D, depends upon normalized measures of energy density and energy density gradients, and it is thermodynamically related to stiffness reduction. From physical observation, D is concurrently linked to local injury within the microstructure of the soft tissue. This field variable, when tracked in finite-element (FE) simulations of the thorax, enables transient monitoring of lung trauma during the course of a blunt impact or a blast event.[18] The authors' novel approach contrasts other state-of-the-art methods whereby lung injury is evaluated a posteriori via calibration.[13,19]

Successful parameterization of the continuum mechanical lung model was demon-

strated in prior works.[5,6,18,20] Only animal data were used in these works, with data on human tissue notably scarce. Animal data were necessarily obtained from sources that considered different species of mammals, since sufficient data for calibration were not available from a single species. This mixing of animal data may not be an overly severe limitation. Differences among certain lung tissue properties (e.g., linearized elastic moduli valid for small deformations) for many mammals are not excessive,[21–28] perhaps because alveolar dimensions, including thickness of septal walls and membranes, are comparable for animals of similar mass.

The equilibrium elastic response of the lung under isotropic expansion and triaxial extension was fit primarily by considering dog experiments, for which data appear most abundant.[21,28–34] Evaluation of the viscoelastic (nonequilibrium) response was performed in the context of pressure relaxation and dynamic simple shear and torsion experiments using experimental data for rabbit[35] and pig[36] lung. Effects of transpulmonary pressure and internal airway pressure on sound speeds predicted by the model were verified using data for horse[37] and rabbit.[27] Trauma data induced by volumetric over-stretching reported from cyclic experiments on rabbit lung[28,38,39] were used to calibrate the threshold and kinetic law for damage-injury under low-rate loading.[6] Shock tube and projectile impact experiments on rabbit lung[28,40] were used to address amplification of damage and injury in the presence of energy gradients due to stress waves with brief rise times in semi-analytical[6,20] and FE[18] calculations.

Human lung tends to exhibit a stiffer mechanical response than dog lung.[41,42] However, the nonlinear elastic parameters of the model in prior work[5,6,20] were primarily calibrated to dog lung data. Furthermore, the initiation thresholds and kinetic factors posited for damage and injury progression in animals[18,28,40] could differ for human subjects. One major purpose of the present report is prescription of alternative parameters for the stiffness and damage components of the model applicable to the human lung. Herein, elastic stiffness parameters are recalibrated based on observations from static biaxial tension data[41] and dynamic shear tests.[43] Effects of these updated parameters, as well as different initial mass densities for the resting state of the lung, are studied for adiabatic uniaxial strain compression, similarly to loading incurred by a uniaxial plane wave. A more detailed account of implementation of the constitutive model as a user subroutine in the `LS-DYNA` software[44] follows next, including numerical algorithms and input file syntax (the latter provided in the

Appendix). Then, performance of the model in LS−DYNA is evaluated for simulations of dynamic impact by a rod to the upper chest region of a representative human torso. Effects of resting lung mass density, a damage kinetic parameter associated with energy gradient amplification, and initial velocity of the rod are examined in parametric studies. Contours of the damage-injury parameter D provide insight into local trauma within each of the lungs. Spatially integrated values are proposed as a global injury criterion. Results are compared with available global injury data from live animal subjects[45] and other thoracic injury criteria[46,47] at comparable impact velocities.

This report is structured as follows. The constitutive theory for the lung parenchyma developed in recent works[5,6,18,20] is reviewed in Section 2. Implementation in the LS-DYNA software is described in Section 3. Trial parameterization for human tissue is reported in Section 4, including analysis of static and dynamic simple shear and uniaxial compression loading. Finite element simulations of dynamic blunt impact to the human torso are discussed in Section 5. Conclusions follow in Section 6. The input file structure for constitutive model parameters (i.e., LS-DYNA card entries for the user material subroutine) is documented in the Appendix.

2. Constitutive Model

The lung material model is summarized in this section. The current presentation is sufficient to render this report, which includes corresponding LS−DYNA documentation for the numerical implementation and input parameters, self-contained. All parameters required by the user material subroutine discussed in Sections 3 and 4 are defined herein. A complete presentation of all model features, with comprehensive theoretical derivations, is available in other published works.[5,6,18,20]

General governing equations of the present theory closely follow those of a nonlinear viscoelastic-damage framework based on QR kinematics.[48,49] The deformation gradient $\boldsymbol{F}$ is decomposed uniquely in the format of a Gram–Schmidt (QR) product of a rotation $\boldsymbol{Q}$ and an upper triangular stretch measure $\boldsymbol{R}$. Strain attributes[50] enter the thermodynamic potentials, and their conjugate scalar stress measures enter the constitutive model. Nonlinear viscoelasticity is addressed in a thermodynamically consistent way[51,52] to the QR framework with strain attributes. A composite internal energy formulation accounts for air compressibility, which crucially affects the effective bulk modulus of the overall structure for dynamic compression.[5,28,37,39,53]

The damage variable is linked to changes in mechanical properties (e.g., stiffness) as well as possible functional impairment such as permeability changes and subsequent edema at low loads and hematoma associated with contusion at more intense loads.[28,39,40,54]

2.1 Kinematics of Finite Deformation

Denoted by $\boldsymbol{X}$ and $\boldsymbol{x}$ are Lagrangian and Eulerian position vectors of a material particle in the respective reference and spatial configurations. Let t denote time. Motions between configurations are

$$\boldsymbol{x} = \boldsymbol{\varphi}(\boldsymbol{X}, t), \qquad \boldsymbol{X} = \boldsymbol{\Phi}(\boldsymbol{x}, t). \tag{1}$$

Particle velocity and acceleration are

$$\boldsymbol{v}(\boldsymbol{X}, t) = \dot{\boldsymbol{x}}(\boldsymbol{X}, t), \qquad \boldsymbol{a}(\boldsymbol{X}, t) = \dot{\boldsymbol{v}}(\boldsymbol{X}, t). \tag{2}$$

The deformation gradient and its inverse are

$$\boldsymbol{F} = \nabla_0 \boldsymbol{\varphi} = \partial \boldsymbol{x} / \partial \boldsymbol{X}, \qquad \boldsymbol{F}^{-1} = \nabla \boldsymbol{\Phi} = \partial \boldsymbol{X} / \partial \boldsymbol{x}. \tag{3}$$

The referential and spatial velocity gradients are

$$\nabla_0 \boldsymbol{v} = \dot{\boldsymbol{F}}, \qquad \nabla \boldsymbol{v} = \dot{\boldsymbol{F}} \boldsymbol{F}^{-1}. \tag{4}$$

A fixed global Cartesian frame with spatial basis vectors $\{\boldsymbol{e}_i\}$, $i = 1, 2, 3$ is used. Let capital indices $J = 1, 2, 3$ denote Lagrangian components. Then

$$\boldsymbol{e}_i = \boldsymbol{e}^i = \delta^i_J \boldsymbol{e}^J = \delta^i_J \boldsymbol{e}_J. \tag{5}$$

The deformation gradient can be decomposed uniquely into the product of a rotation $\boldsymbol{Q}$ and upper triangular matrix $\boldsymbol{R}$, where the latter is known as the Laplace stretch[55]:

$$\boldsymbol{F} = \boldsymbol{Q}\boldsymbol{R} = Q^i_K R^K_J \boldsymbol{e}_i \otimes \boldsymbol{e}^J; \qquad \boldsymbol{Q}^{-1} = \boldsymbol{Q}^{\mathrm{T}}, \quad \det \boldsymbol{Q} = +1. \tag{6}$$

In matrix form,

$$\boldsymbol{R} = \begin{bmatrix} R_{11} & R_{12} & R_{13} \\ 0 & R_{22} & R_{23} \\ 0 & 0 & R_{33} \end{bmatrix} = \begin{bmatrix} a & a\gamma & a\beta \\ 0 & b & b\alpha \\ 0 & 0 & c \end{bmatrix} = \begin{bmatrix} a & 0 & 0 \\ 0 & b & 0 \\ 0 & 0 & c \end{bmatrix} \begin{bmatrix} 1 & \gamma & \beta \\ 0 & 1 & \alpha \\ 0 & 0 & 1 \end{bmatrix} = \boldsymbol{\Lambda\Gamma}. \quad (7)$$

Physically descriptive deformation measures are the three positive elongation ratios a, b, c that enter the extension matrix $\boldsymbol{\Lambda}$ and the three shear magnitudes α, β, γ that enter the simple shear matrix $\boldsymbol{\Gamma}$.

Volume change, with $\mathrm{d}V$ and $\mathrm{d}V_0$ local spatial and initial volume elements, is measured by

$$J = \mathrm{d}V/\mathrm{d}V_0 = \det \boldsymbol{R} = \det \boldsymbol{\Lambda} = abc. \quad (8)$$

Parameters $a, b, c, \alpha, \beta, \gamma$ are physical attributes.[56–58] Let

$$\boldsymbol{C} = \boldsymbol{F}^{\mathrm{T}}\boldsymbol{F} = \boldsymbol{R}^{\mathrm{T}}\boldsymbol{R} = C_{IJ}\boldsymbol{e}^I \otimes \boldsymbol{e}^J = F^i_I \delta_{ij} F^j_J \boldsymbol{e}^I \otimes \boldsymbol{e}^J = R^K_I \delta_{KL} R^L_J \boldsymbol{e}^I \otimes \boldsymbol{e}^J \quad (9)$$

denote the symmetric right Cauchy–Green deformation tensor. Nonzero components of $\boldsymbol{R} = R_{IJ}\boldsymbol{e}^I \otimes \boldsymbol{e}^J$ are obtained explicitly from the components C_{IJ} by[59]

$$\begin{aligned} &R_{11} = \sqrt{C_{11}}, \quad R_{12} = C_{12}/R_{11}, \quad R_{13} = C_{13}/R_{11}, \quad R_{22} = \sqrt{C_{22} - (R_{12})^2}, \\ &R_{23} = (C_{23} - R_{12}R_{13})/R_{22}, \qquad R_{33} = \sqrt{C_{33} - (R_{13})^2 - (R_{23})^2}. \end{aligned} \quad (10)$$

Elongations and shears are

$$a = R_{11}, \quad b = R_{22}, \quad c = R_{33}; \qquad \alpha = \frac{R_{23}}{R_{22}}, \quad \beta = \frac{R_{13}}{R_{11}}, \quad \gamma = \frac{R_{12}}{R_{11}}. \quad (11)$$

The inverse of $\boldsymbol{R}$ is also upper triangular:

$$\boldsymbol{R}^{-1} = \boldsymbol{\Gamma}^{-1}\boldsymbol{\Lambda}^{-1} = \begin{bmatrix} 1/a & -\gamma/b & (\alpha\gamma - \beta)/c \\ 0 & 1/b & -\alpha/c \\ 0 & 0 & 1/c \end{bmatrix}. \quad (12)$$

With Eq. 12, $\boldsymbol{Q} = \boldsymbol{F}\boldsymbol{R}^{-1}$ can be calculated by matrix multiplication. Given F^i_J, no eigenvalue analysis is needed for a QR decomposition. Compatibility conditions have been analyzed in the context of the QR decomposition in two[60] and three[61]

dimensions. Unless $\boldsymbol{Q}$ is homogeneous, the intermediate space attained from the reference configuration via a push-forward with $\boldsymbol{R}$ is anholonomic.[62,63]

Index numbers $1, 2, 3$ to the $\{\boldsymbol{e}_i\}$ should be assigned carefully when the QR decomposition is used. Let the $\{\boldsymbol{e}_i\}$ be rotated by $\boldsymbol{Q}$. An ideal choice of bases considers the properties[64] that the direction aligned with the rotated 1-axis and the direction normal to the rotated 1-2-plane remain invariant under a tangent mapping by upper triangular transformation $\boldsymbol{R}$. It is assumed henceforth that the $\{\boldsymbol{e}_i\}$ have been ideally labeled such that the rotated 1-direction aligns with the axis of minimal transverse shear. A pivoting algorithm for coordinate indexing to achieve the corresponding upper triangular dominance of $\boldsymbol{R}$ is elaborated elsewhere.[58,65]

The spatial velocity gradient obeys

$$\nabla \boldsymbol{v} = \dot{\boldsymbol{F}}\boldsymbol{F}^{-1} = \dot{\boldsymbol{Q}}\boldsymbol{Q}^{-1} + \boldsymbol{Q}\dot{\boldsymbol{R}}\boldsymbol{R}^{-1}\boldsymbol{Q}^{-1} = \boldsymbol{\Omega} + \boldsymbol{Q}\boldsymbol{\eta}\boldsymbol{Q}^{-1}, \tag{13}$$

where $\boldsymbol{\Omega}$ is skew and the rate contribution from the Laplace stretch is embodied by

$$\boldsymbol{\eta} = \dot{\boldsymbol{R}}\boldsymbol{R}^{-1} = \begin{bmatrix} \dot{a}/a & a\dot{\gamma}/b & a(\dot{\beta} - \alpha\dot{\gamma})/c \\ 0 & \dot{b}/b & b\dot{\alpha}/c \\ 0 & 0 & \dot{c}/c \end{bmatrix}. \tag{14}$$

Let a_0, b_0, c_0 and $\alpha_0, \beta_0, \gamma_0$ denote values of a, b, c and α, β, γ in a reference state corresponding to time instant $t = t_0$. A vector consisting of seven strain attributes ϵ_i, $i = 0, \ldots, 6$ is defined, along with corresponding rates $\dot{\epsilon}_i$, as

$$\{\epsilon_i\} = \begin{Bmatrix} \epsilon_0 \\ \epsilon_1 \\ \epsilon_2 \\ \epsilon_3 \\ \epsilon_4 \\ \epsilon_5 \\ \epsilon_6 \end{Bmatrix} = \begin{Bmatrix} \ln(abc/a_0b_0c_0) \\ \frac{1}{3}\ln(ab_0/a_0b) \\ \frac{1}{3}\ln(bc_0/b_0c) \\ \frac{1}{3}\ln(ca_0/c_0a) \\ \gamma - \gamma_0 \\ \alpha - \alpha_0 \\ \beta - \beta_0 \end{Bmatrix}, \qquad \{\dot{\epsilon}_i\} = \begin{Bmatrix} \dot{\epsilon}_0 \\ \dot{\epsilon}_1 \\ \dot{\epsilon}_2 \\ \dot{\epsilon}_3 \\ \dot{\epsilon}_4 \\ \dot{\epsilon}_5 \\ \dot{\epsilon}_6 \end{Bmatrix} = \begin{Bmatrix} \dot{a}/a + \dot{b}/b + \dot{c}/c \\ \frac{1}{3}(\dot{a}/a - \dot{b}/b) \\ \frac{1}{3}(\dot{b}/b - \dot{c}/c) \\ \frac{1}{3}(\dot{c}/c - \dot{a}/a) \\ \dot{\gamma} \\ \dot{\alpha} \\ \dot{\beta} \end{Bmatrix}. \tag{15}$$

Only six of the seven strain attributes in Eq. 15 are independent kinematic variables since

$$\epsilon_1 + \epsilon_2 + \epsilon_3 = 0 \quad \Rightarrow \quad \dot{\epsilon}_1 + \dot{\epsilon}_2 + \dot{\epsilon}_3 = 0. \tag{16}$$

A logarithmic measure of the dilatation is ϵ_0. When $a_0 = b_0 = c_0 = 1$ is chosen for the datum state, $\epsilon_0 = \ln J$ follows from Eq. 8. This choice is used henceforth, as are $\alpha_0 = \beta_0 = \gamma_0 = 0$. Such choices imply that the initial state is "undeformed". Logarithmic squeeze modes are $\epsilon_1, \epsilon_2, \epsilon_3$; these are collectively isochoric, though isolated squeeze modes do not preserve volume. Simple shears are $\epsilon_4, \epsilon_5, \epsilon_6$; these individually and collectively preserve volume.

2.2 Stress Power, Conservation Laws, and Entropy Production

Denote by $\boldsymbol{\sigma}$, $\boldsymbol{k}$, $\boldsymbol{s}$, and $\boldsymbol{P}$ the Cauchy, Kirchhoff, rotated Kirchhoff, and first Piola–Kirchhoff stress tensors, respectively. These stress tensors are related by

$$\boldsymbol{\sigma} = J^{-1}\boldsymbol{P}\boldsymbol{F}^{\mathrm{T}} = J^{-1}\boldsymbol{k} = J^{-1}\boldsymbol{Q}\boldsymbol{s}\boldsymbol{Q}^{-1}. \tag{17}$$

The Cauchy pressure, positive in compression, is

$$p = -\frac{1}{3}\mathrm{tr}\boldsymbol{\sigma} = -\frac{1}{3J}\mathrm{tr}\boldsymbol{k} = -\frac{1}{3J}\mathrm{tr}\boldsymbol{s}. \tag{18}$$

The stress power per unit reference volume is

$$\boldsymbol{P} : \dot{\boldsymbol{F}} = J\boldsymbol{\sigma} : \nabla\boldsymbol{v} = \boldsymbol{k} : \nabla\boldsymbol{v} = \boldsymbol{s} : \boldsymbol{\eta} = \sum_{i=0}^{6} \hat{\tau}_i \dot{\epsilon}_i. \tag{19}$$

The rightmost term is the stress power in terms of rates of strain attributes of Eq. 15 and their scalar stress conjugates.[48,49,58]

Define $\{\hat{\tau}_i\}$, $i = 0, \ldots, 6$ in terms of $s_{\alpha\beta}$ as[58]

$$\{\hat{\tau}_i\} = \begin{Bmatrix} \hat{\tau}_0 \\ \hat{\tau}_1 \\ \hat{\tau}_2 \\ \hat{\tau}_3 \\ \hat{\tau}_4 \\ \hat{\tau}_5 \\ \hat{\tau}_6 \end{Bmatrix} = \begin{Bmatrix} \frac{1}{3}(s_{11} + s_{22} + s_{33}) \\ s_{11} - s_{22} \\ s_{22} - s_{33} \\ s_{33} - s_{11} \\ (a/b)s_{21} - \alpha(a/c)s_{31} \\ (b/c)s_{32} \\ (a/c)s_{31} \end{Bmatrix}. \tag{20}$$

Negative pressure per unit reference volume is $\hat{\tau}_0 = -Jp$. Normal stress differences are $\hat{\tau}_1, \hat{\tau}_2, \hat{\tau}_3$. Shear stresses are $\hat{\tau}_4, \hat{\tau}_5, \hat{\tau}_6$. Normal stress differences conjugate to

squeeze modes of strain obey

$$\hat{\tau}_1 + \hat{\tau}_2 + \hat{\tau}_3 = 0. \tag{21}$$

Let ρ and ρ_0 be spatial and initial mass densities of the material. Body force per unit initial volume is $\boldsymbol{b}$. Local balance equations for mass, linear momentum, and angular momentum are the usual forms from continuum mechanics[66,67]:

$$\dot{\rho} + \rho \nabla \cdot \boldsymbol{v} = 0, \qquad \nabla_0 \cdot \boldsymbol{P} + \boldsymbol{b} = \rho_0 \boldsymbol{a}, \qquad \boldsymbol{P}\boldsymbol{F}^{\mathrm{T}} = \boldsymbol{F}\boldsymbol{P}^{\mathrm{T}}. \tag{22}$$

Thermodynamic potentials, measured per unit initial volume, include internal energy density U, Helmholtz free energy density Ψ, and entropy density η. These are related conventionally via

$$U = \Psi + T\eta. \tag{23}$$

The absolute temperature is $T > 0$. The heat flux vector in the reference configuration is $\boldsymbol{q}$, and a scalar point heat source per unit volume is r. The local balance of energy is

$$\dot{U} = \boldsymbol{P} : \dot{\boldsymbol{F}} - \nabla_0 \cdot \boldsymbol{q} + r. \tag{24}$$

Local entropy production inequalities include

$$\dot{\eta} \geq \frac{1}{T}\left(r + \frac{\boldsymbol{q} \cdot \nabla_0 T}{T} - \nabla_0 \cdot \boldsymbol{q}\right), \qquad \boldsymbol{P} : \dot{\boldsymbol{F}} - \frac{\boldsymbol{q} \cdot \nabla_0 T}{T} \geq \dot{\Psi} + \dot{T}\eta. \tag{25}$$

2.3 Generic Constitutive Laws

Thermodynamic potentials Ψ or U depend on temperature (T) or entropy (η), internal state variables, and strain attributes. Let $\{\chi_i^\alpha\}$ be a set of dimensionless, strain-like scalar variables associated with viscoelasticity, where $i = 0, \ldots, 6$ and $\alpha = 1, \ldots, m$, with m a discrete number of relaxation times. Denote by $D \in [0, 1]$ an internal state variable linked to damage processes. Strain attributes and viscoelastic state variables comprise the column vectors

$$\boldsymbol{\epsilon} = [\epsilon_0, \epsilon_1, \epsilon_2, \epsilon_3, \epsilon_4, \epsilon_5, \epsilon_6]^{\mathrm{T}}, \qquad \boldsymbol{\chi}^\alpha = [\chi_0^\alpha, \chi_1^\alpha, \chi_2^\alpha, \chi_3^\alpha, \chi_4^\alpha, \chi_5^\alpha, \chi_6^\alpha]^{\mathrm{T}}. \tag{26}$$

Free and internal energy densities are assigned the following functional forms:

$$\Psi = \Psi(\boldsymbol{\epsilon}, T, \boldsymbol{\chi}^\alpha, D), \qquad U = U(\boldsymbol{\epsilon}, \eta, \boldsymbol{\chi}^\alpha, D). \tag{27}$$

Using Eq. 27 in the second of Eq. 25 gives

$$\sum_{i=0}^{6} \hat{\tau}_i \dot{\epsilon}_i - \frac{\partial \Psi}{\partial \boldsymbol{\epsilon}} \cdot \dot{\boldsymbol{\epsilon}} - \left(\eta + \frac{\partial \Psi}{\partial \eta} \right) \dot{T} - \sum_{\alpha=1}^{m} \frac{\partial \Psi}{\partial \boldsymbol{\chi}^\alpha} \cdot \dot{\boldsymbol{\chi}}^\alpha - \frac{\partial \Psi}{\partial D} \dot{D} - \frac{\boldsymbol{q} \cdot \nabla_0 T}{T} \geq 0. \quad (28)$$

Stress power can be written, using Eqs. 16 and 21, in terms of components of $\dot{\boldsymbol{\epsilon}}$:

$$\sum_{i=0}^{6} \hat{\tau}_i \dot{\epsilon}_i = \sum_{i=0}^{2} \hat{\tau}_i \dot{\epsilon}_i + (\hat{\tau}_1 + \hat{\tau}_2)(\dot{\epsilon}_1 + \dot{\epsilon}_2) + \sum_{i=4}^{6} \hat{\tau}_i \dot{\epsilon}_i. \quad (29)$$

The following thermoelastic constitutive equations are inferred from Eq. 28 to maintain admissibility for stresses

$$\begin{aligned} \hat{\tau}_0 &= \frac{\partial \Psi}{\partial \epsilon_0}, \quad \hat{\tau}_1 = \frac{\partial \Psi}{\partial \epsilon_1}, \quad \hat{\tau}_2 = \frac{\partial \Psi}{\partial \epsilon_2}, \quad \hat{\tau}_3 = \frac{\partial \Psi}{\partial \epsilon_3}, \\ \hat{\tau}_4 &= \frac{\partial \Psi}{\partial \epsilon_4}, \quad \hat{\tau}_5 = \frac{\partial \Psi}{\partial \epsilon_5}, \quad \hat{\tau}_6 = \frac{\partial \Psi}{\partial \epsilon_6}; \end{aligned} \quad (30)$$

and entropy

$$\eta = -\frac{\partial \Psi}{\partial T}. \quad (31)$$

The first of Eq. 30 corresponds to $p = -J^{-1}\hat{\tau}_0 = -\frac{\partial \Psi}{\partial J}$. For Eq. 30 to always apply under Eqs. 16 and 21, free energy Ψ must be specified consistently with

$$\frac{\partial \Psi}{\partial \epsilon_1} + \frac{\partial \Psi}{\partial \epsilon_2} + \frac{\partial \Psi}{\partial \epsilon_3} = 0. \quad (32)$$

Partial differentiation with respect to ϵ_i is performed with ϵ_j fixed for all $i \neq j$, regardless of Eq. 16. The residual dissipation inequality is

$$-\sum_{\alpha=1}^{m} \frac{\partial \Psi}{\partial \boldsymbol{\chi}^\alpha} \cdot \dot{\boldsymbol{\chi}}^\alpha - \frac{\partial \Psi}{\partial D} \dot{D} - \frac{\boldsymbol{q} \cdot \nabla_0 T}{T} \geq 0. \quad (33)$$

The seven-element column vector of stress variables conjugate to strain attributes is

$$\hat{\boldsymbol{\tau}} = [\hat{\tau}_0, \hat{\tau}_1, \hat{\tau}_2, \hat{\tau}_3, \hat{\tau}_4, \hat{\tau}_5, \hat{\tau}_6]^{\mathrm{T}}. \quad (34)$$

Concisely, this is related to strain derivatives of free energy according to

$$\hat{\boldsymbol{\tau}} = \partial_{\boldsymbol{\epsilon}} \Psi = \frac{\partial \Psi}{\partial \boldsymbol{\epsilon}}. \tag{35}$$

If seven components in Eq. 30 are known, then the symmetric physical stress tensor $\boldsymbol{s}$ is, from inversion of Eq. 20,

$$\begin{aligned} &s_{11} = \hat{\tau}_0 + \frac{1}{3}(\hat{\tau}_1 - \hat{\tau}_3), \quad s_{22} = \hat{\tau}_0 + \frac{1}{3}(\hat{\tau}_2 - \hat{\tau}_1), \quad s_{33} = \hat{\tau}_0 + \frac{1}{3}(\hat{\tau}_3 - \hat{\tau}_2), \\ &s_{12} = s_{21} = \frac{b}{a}(\hat{\tau}_4 + \alpha \hat{\tau}_6), \quad s_{23} = s_{32} = \frac{c}{b}\hat{\tau}_5, \quad s_{13} = s_{31} = \frac{c}{a}\hat{\tau}_6. \end{aligned} \tag{36}$$

Other stress tensors such as Cauchy stress $\boldsymbol{\sigma}$ can be obtained from $\boldsymbol{s}$ using Eq. 17. Thermoelastic constitutive equations in terms of internal energy are derived similarly[48,49]:

$$\begin{aligned} &\hat{\tau}_0 = \frac{\partial U}{\partial \epsilon_0}, \quad \hat{\tau}_1 = \frac{\partial U}{\partial \epsilon_1} \quad \hat{\tau}_2 = \frac{\partial U}{\partial \epsilon_2} \quad \hat{\tau}_3 = \frac{\partial U}{\partial \epsilon_3}, \\ &\hat{\tau}_4 = \frac{\partial U}{\partial \epsilon_4}, \quad \hat{\tau}_5 = \frac{\partial U}{\partial \epsilon_5}, \quad \hat{\tau}_6 = \frac{\partial U}{\partial \epsilon_6}; \qquad T = \frac{\partial U}{\partial \eta}. \end{aligned} \tag{37}$$

Constraints analogous to Eq. 32 are imposed on the strain derivatives of internal energy U: $\sum_{i=1,2,3} \partial U / \partial \epsilon_i = 0$.

Let $c(\boldsymbol{\epsilon}, T, \boldsymbol{\chi}^\alpha, D)$ denote specific heat per unit reference volume at constant deformation, where

$$c = \frac{\partial U}{\partial T} = T \frac{\partial \eta}{\partial T} = -T \frac{\partial^2 \Psi}{\partial T^2}. \tag{38}$$

The following temperature evolution equation can be derived from the local balance of energy:

$$\begin{aligned} c\dot{T} = &- \sum_{\alpha=1}^{m} (\partial \Psi / \partial \boldsymbol{\chi}^\alpha) \cdot \dot{\boldsymbol{\chi}}^\alpha - (\partial \Psi / \partial D)\dot{D} - \nabla_0 \cdot \boldsymbol{q} + r \\ &+ T \left[(\partial^2 \Psi / \partial \boldsymbol{\epsilon} \partial T) : \dot{\boldsymbol{\epsilon}} + \sum_{\alpha=1}^{m} (\partial^2 \Psi / \partial T \partial \boldsymbol{\chi}^\alpha) \cdot \dot{\boldsymbol{\chi}}^\alpha + (\partial^2 \Psi / \partial T \partial D)\dot{D} \right]. \end{aligned} \tag{39}$$

Thermal stress coefficients $\boldsymbol{\kappa}$ and Grüneisen coefficients $\boldsymbol{g}$ are defined as

$$\boldsymbol{\kappa} = -\frac{\partial^2 \Psi}{\partial \boldsymbol{\epsilon} \partial T} = c\boldsymbol{g}. \tag{40}$$

Isothermal and isentropic, respectively, second-order thermodynamic elastic coefficients (not necessarily constants) are

$$\mathbf{C}^T = \frac{\partial^2 \Psi}{\partial \boldsymbol{\epsilon} \partial \boldsymbol{\epsilon}}, \qquad \mathbf{C}^\eta = \frac{\partial^2 U}{\partial \boldsymbol{\epsilon} \partial \boldsymbol{\epsilon}}. \tag{41}$$

Denote thermal expansion coefficients by $\boldsymbol{A} = \partial \boldsymbol{\epsilon} / \partial T$, with partial differentiation taken at constant stress and constant internal state. Denote specific heat at constant stress by c^s. Relationships among thermodynamic coefficients include

$$\boldsymbol{\kappa} = \boldsymbol{A} : \mathbf{C}^T, \qquad c^s - c = T \boldsymbol{A} : \boldsymbol{\kappa}, \qquad \mathbf{C}^\eta = \mathbf{C}^T + \frac{T}{c} \boldsymbol{\kappa} \otimes \boldsymbol{\kappa}. \tag{42}$$

Define conjugate thermodynamic forces to internal state variables as the negative derivatives

$$\bar{\boldsymbol{\zeta}}^\alpha = -\frac{\partial \Psi}{\partial \boldsymbol{\chi}^\alpha}, \qquad \bar{F} = -\frac{\partial \Psi}{\partial D}. \tag{43}$$

Substitution of Eqs. 40 and 43 into Eq. 39 gives another local energy balance:

$$c\dot{T} = -T\boldsymbol{\kappa} : \dot{\boldsymbol{\epsilon}} + \sum_{\alpha=1}^{m} [\bar{\boldsymbol{\zeta}}^\alpha - T(\partial \bar{\boldsymbol{\zeta}}^\alpha / \partial T)] \cdot \dot{\boldsymbol{\chi}}^\alpha + [\bar{F} - T(\partial \bar{F} / \partial T)] \dot{D} - \nabla_0 \cdot \boldsymbol{q} + r. \tag{44}$$

Assume that dissipation from conduction is always nonnegative; the internal dissipation inequality and entropy production rate are then

$$\mathfrak{D} = \sum_{\alpha=1}^{m} \bar{\boldsymbol{\zeta}}^\alpha \cdot \dot{\boldsymbol{\chi}}^\alpha + \bar{F} \dot{D} \geq 0, \qquad T\dot{\eta} = \mathfrak{D} - \nabla_0 \cdot \boldsymbol{q} + r. \tag{45}$$

2.4 Internal Energy Formulation for Air-Tissue Response

A constitutive formulation for static and dynamic loading of the lung based on the internal energy potential U is now developed. This model is preferred for compressive stress states and high strain rates, and it is ideal for isentropic problems such as elastic wave propagation. This model accounts for compressibility of the air inside the lung, and thus can be used to model adiabatic shock loading processes in which air does not have time to redistribute among or escape from the alveoli.

A material element consists of dense lung tissue, surface liquid, and air inside alveoli. Under slow deformation processes, air has time to move throughout the

microstructure—or when the entire lung is considered, enter and exit through open trachea—and only the tissue network and surface liquid affect the stiffness. Under very rapid loading (or if the trachea is artificially sealed), air does not have time to redistribute or escape, and compressibility of the air affects the response in conjunction with the dense tissue and liquid phase.[53] The present model addresses only the two extreme regimes: very slow and very fast loading corresponding to an open-cell and closed-cell model for the effective bulk modulus, respectively.[37]

By definition,[28,31,32,68] transpulmonary pressure p_{tp} is the difference between the internal airway pressure in the lung (or inside an internally pressurized element of lung tissue) denoted by p_a and the pleural pressure p_{pl}, which is the external pressure acting on the outer surface of the lung or an element of it:

$$-p = p_{tp} = p_a - p_{pl}. \tag{46}$$

Effects of tension and curvature in the pleural membrane[31,32] are embedded in p_{pl} and not are resolved explicitly here. Both p_a and p_{pl} are positive in compression. In vivo, pressure in the intrapleural space is less than airway pressure (i.e., negative relative to atmosphere) to keep the lung from collapsing due to its intrinsic surface tension. Under normal breathing cycles, lung tissue remains perpetually in a tensile stress state,[69] whereby the tissue pressure (elastic + surface tension contributions) is $p < 0$ and $p_{tp} > 0$. Typically, $p_a \approx 1$ atm $= 101.3$ kPa = 1.033×10^3 cm H_2O.

Two damage degradation functions are $\bar{f} \in [0,1]$ and $f \in [0,1]$. Function f degrades the stiffness in pure and simple shear. Function $\bar{f}$ degrades the bulk stiffness, and $\bar{f}(D) \geq f(D)$ is imposed conditionally later such that under rapid compression, the tangent bulk modulus cannot fall below that of air alone in the initial state. The purely entropic internal energy accounting for specific heat is u; this is assumed unaffected by damage. The following form of U in the second of Eq. 27 is thus invoked[6,18]:

$$\begin{aligned} U(\boldsymbol{\epsilon},\eta,\boldsymbol{\chi}^1,D) &= \bar{f}(D)[U_0^V(\boldsymbol{\epsilon},\eta,\boldsymbol{\chi}^1)] + f(D)[U_0^\mu(\boldsymbol{\epsilon},\boldsymbol{\chi}^1) + U_0^G(\boldsymbol{\epsilon},\boldsymbol{\chi}^1)] + u(\eta) \\ &= \bar{f}(D)[U_0^{V\infty}(\epsilon_0,\eta) + \Upsilon_0^V(\epsilon_0,\chi_0^1)] \\ &\quad + f(D)[U_0^{\mu\infty}(\boldsymbol{\epsilon}) + U_0^{G\infty}(\boldsymbol{\epsilon}) + \Upsilon_0^\mu(\boldsymbol{\epsilon},\boldsymbol{\chi}^1) + \Upsilon_0^G(\boldsymbol{\epsilon},\boldsymbol{\chi}^1)] + u(\eta). \end{aligned} \tag{47}$$

Attention is limited to consideration of a single viscous relaxation mode corre-

sponding to $\alpha = 1$ in Eq. 27. Equilibrium thermoelastic internal energy, including strain energy and coupling from thermal expansion, is $U_0^\infty = U_0^{V\infty} + U_0^{\mu\infty} + U_0^{G\infty}$, partitioned into contributions from dilatation, squeeze, and simple shear. Configurational internal energy associated with viscoelasticity, partitioned similarly, is $\Upsilon_0 = \Upsilon_0^V + \Upsilon_0^\mu + \Upsilon_0^G$. Thermoelastic and viscous contributions also simply sum as can be inferred from Eq. 47:

$$\begin{gathered} U_0 = U_0^V + U_0^\mu + U_0^G; \\ U_0^V = U_0^{V\infty} + \Upsilon_0^V, \qquad U_0^\mu = U_0^{\mu\infty} + \Upsilon_0^\mu, \qquad U_0^G = U_0^{G\infty} + \Upsilon_0^G. \end{gathered} \tag{48}$$

For the open-cell model, the stress supported by the continuum material element is that sustained by the tissue and its surface air–liquid interface, if not saline-washed. A material element is considered to occupy a stress-free reference state[31,32] when undeformed ($\boldsymbol{F} = \mathbf{1}$ and $J = 1$) and in the absence of surface tension at the air–liquid interface, wherein its mass density is ρ_0 and entropy is η_0. Surface tension will produce tensile pressure at $J = 1$. Transpulmonary pressure p_{tp} is equal to the negative of pressure supported by continuum element, related to internal airway pressure p_a and pleural/external pressure p_{pl} via Eq. 46. Neither p_a nor p_{pl} need be known explicitly to use the open-cell model. When one is given (e.g., $p_a = 1$ atm), then the other (e.g., p_{pl}) can be computed a posteriori once $p = -p_{tp}$ is obtained from the constitutive model. All pressures entering Eq. 46 are referred in this work to a datum of absolute zero (vacuum). Accordingly, $p_a \geq 0$ since air alone cannot sustain tensile pressure, at least in the context of ideal gas models.[70]

The closed-cell model is more complicated. A continuum material element consists of the dense tissue phase (solid + liquid) as well as the internal air phase (gas). Volume fractions occupied by each phase in the reference state are denoted by v_t and v_a for dense tissue and air, respectively, related by $v_t + v_a = 1$. The reference state of the effective continuum element for which $\boldsymbol{F} = \mathbf{1}$, $J = 1$, $\rho = \rho_0$, and $\eta = \eta_0$ is defined as follows. The continuum stress vanishes, and thus $p = 0$, for this element at the reference state in the absence of surface tension. The internal airway pressure at the reference state is imposed a priori as $p_a = p_{a0} > 0$, where a vacuum airway state is not considered to avoid singularities later. Thus, from Eq. 46, the pleural pressure, positive in compression, for the reference state at $J = 1$ is $p_{pl} = p + p_a = -K_0 + p_{a0}$, where K_0 is the surface tension. In the absence of surface tension, pleural pressure and internal airway pressure balance to ensure the

reference state is stress-free.

Material coefficients entering the internal energy function U_0 depend on v_t and p_{a0}, which are regarded as fixed initial values during the solution of any boundary value problem. This does not imply that internal airway pressure p_a remains constant during the time history of deformation. However, pressures and other state functions (e.g., other stress components, temperatures, entropies) are not resolved explicitly within each phase by the present composite model during the deformation process.

Equilibrium thermoelastic internal energy depends explicitly on three functions of the strain attributes of Eq. 15, denoted by ξ_i, $i = 1, 2, 3$ and defined as

$$\begin{aligned} \xi_1 &= \epsilon_0 = \ln J, \\ \xi_2 &= (\epsilon_1)^2 + (\epsilon_2)^2 + (\epsilon_3)^2, \\ \xi_3 &= (\epsilon_4)^2 + (\epsilon_5)^2 + (\epsilon_6)^2 = \alpha^2 + \beta^2 + \gamma^2. \end{aligned} \tag{49}$$

This choice represents a three-mode pseudo-isotropic theory in the sense of Freed and Clayton.[48,49,56,58] A convenient property of the form $U_0^\infty(\xi_1, \xi_2, \xi_3, \eta)$ is that the thermoelastic internal energy analog of Eq. 32 is identically satisfied through Eq. 16.

The equilibrium thermoelastic strain energy density per unit reference volume is prescribed as follows:

$$\begin{aligned} U_0^\infty(\xi_1, \xi_2, \xi_3, \eta) = \frac{1}{2}\frac{\bar{B}_0^\eta}{c_1}\{\exp[c_1(\xi_1)^2] - 1\} - g_0 T_0 \eta \xi_1 + K_0 \xi_1 \\ + 3\frac{\mu_0}{c_2}\{\exp[c_2\xi_2] - 1\}\left[1 - \frac{B_0^T}{\mu_0}\mu_0'\xi_1\right] \\ + \frac{1}{2}\frac{G_0}{c_3}\{\exp[c_3\xi_3] - 1\}\left[1 - \frac{B_0^T}{G_0}G_0'\xi_1\right]. \end{aligned} \tag{50}$$

Thermoelastic strain energy is partitioned into contributions from dilatation, squeeze, and simple shear:

$$U_0^\infty = U_0^{V\infty} + U_0^{\mu\infty} + U_0^{G\infty}; \tag{51}$$

$$
\begin{aligned}
U_0^{V\infty} &= \frac{1}{2}\frac{\bar{B}_0^{\eta}}{c_1}\{\exp[c_1(\xi_1)^2]-1\} + K_0\xi_1 - g_0T_0\xi_1\eta, \\
U_0^{\mu\infty} &= 3\frac{\mu_0}{c_2}\{\exp[c_2\xi_2]-1\}\left[1-\frac{B_0^T}{\mu_0}\mu_0'\xi_1\right], \\
U_0^{G\infty} &= \frac{1}{2}\frac{G_0}{c_3}\{\exp[c_3\xi_3]-1\}\left[1-\frac{B_0^T}{G_0}G_0'\xi_1\right].
\end{aligned}
\tag{52}
$$

Denoted by $\bar{B}_0^{\eta}$ is the effective isentropic bulk modulus, μ_0 the shear modulus for pure shear, and G_0 the shear modulus for simple shear, all corresponding to tangent moduli at the undeformed reference state for equilibrium quasi-static deformation (i.e., no viscoelasticity), in the absence of damage.

The linear shear moduli are identical in value and definition to μ_0 and G_0 of a free energy-based formulation,[6,20] since only the bulk modulus, and not squeeze and shear moduli, differ under isothermal and isentropic deformation in isotropic thermoelastic solids, as readily verified via Eqs. 41 and 42. The datum value of entropy at the reference state is chosen as $\eta_0 = 0$ for simplicity. Temperature at the reference state is the constant T_0, usually assigned as body temperature. The isentropic pressure derivatives of the shear moduli at the reference state are μ_0' and G_0'. The isothermal bulk modulus is B_0^T. Dimensionless higher-order elastic constants corresponding to dilatation, squeeze, and simple shear are c_1, c_2, and c_3. These nonlinear elastic coefficients enable Fung-type exponential stiffening evident in many kinds of soft biological tissues.[28,71,72] The simple one-parameter model of surface tension (K_0 =constant) does not distinguish between open- and closed-cell regimes or between isothermal and isentropic loading.

The first term in Eq. 50 accounts for the isentropic pressure–volume response and contains the isentropic bulk modulus at the reference state, $\bar{B}_0^{\eta}$. The second term in Eq. 50 accounts for thermoelastic coupling and contains the Grüneisen parameter at the reference state, g_0. These two coefficients are defined shortly in the text. The purely entropic contribution to internal energy in Eq. 47 is defined in terms of specific heat at constant volume c_0, also specified fully later, as follows:

$$
u(\eta) = T_0\eta\left[1+\frac{1}{2}\frac{\eta}{c_0}\right]. \tag{53}
$$

Denote by ρ_t the constant mass density of the condensed tissue phase at the reference state. Denote by ρ_{a0} the mass density of the internal air at the reference state.

Treating air as an ideal gas, $\rho_{a0} = (p_{a0}/p_1)\rho_{a1}$, where $\rho_{a1} = 1.2 \times 10^{-3}$ g/cm^3 is the mass density of air at room temperature T_0 and $p_1 = 1$ atm. The reference mass density of the composite lung (condensed tissue + gas phases) is

$$\rho_0(v_t, p_{a0}) = v_t \cdot \rho_t + (1 - v_t) \cdot \rho_{a0}(p_{a0}). \tag{54}$$

The mass density of the composite lung ρ_{00} is first measured in air at a given internal pressure $p_{a0} = p_{pl}$ (i.e., at zero transpulmonary pressure). The reference state mass density ρ_0 is then found from mass conservation as $\rho_0 J_0 = \rho_{00} J_{00}$, where J_{00} is the calculated contraction due to surface tension K_0 computed using the static spherical response.[6,20] For properties of dog lung,[5,6,20] $J_{00} = 0.9245$ is obtained. Note that $J_0 = 1$ by definition in the undeformed reference state. The volume fraction of tissue v_t is lastly obtained by an implicit solution of Eq. 54. Afterwards, ρ_0 and v_t can be treated as constants for a given lung sample and set of initial conditions.

Mixture theory is used to estimate the coefficient of thermal expansion for the composite lung, denoted by A_0, and the specific heat per unit reference *volume* at constant volume, denoted by c_0. Denote by subscripts $(\cdot)_t$ and $(\cdot)_a$ quantities for dense tissue and air phases at the reference state at temperature T_0, and denote by C the specific heat per unit *mass* at constant volume. Then,

$$A_0 = v_t \cdot A_t + (1 - v_t) \cdot A_a, \qquad c_0 = v_t \rho_t C_t + (1 - v_t)\rho_{a0} \cdot C_a. \tag{55}$$

For an ideal gas, $A_a = 1/T_0$, and the specific heat per unit mass of air is reasonably constant at moderate excursions from room temperature,[70] here $C_a = 718$ J/kg·K.

The definition of the effective isentropic bulk modulus at the undeformed reference state depends on the loading regime, where an open-cell model is used for static to moderate volumetric strain rates, and a closed-cell model for high rates wherein air does not have time to flow through or exit the alveolar microstructure. Specifically,

$$\bar{B}_0^\eta = \begin{cases} B_0^\eta = B_0^T(1 + g_0 A_0 T_0) & \text{(open-cell model)}, \\ \left[\frac{v_t}{B_t^\eta} + \frac{1 - v_t}{\Gamma p_{a0}}\right]^{-1} & \text{(closed-cell model)}. \end{cases} \tag{56}$$

The definition of the open-cell modulus is a standard thermodynamic identity.[67,70] Recall that B_0^T is the open-cell isothermal bulk modulus for quasi-static extension. The closed-cell modulus results from a referential volume average of the compli-

ance of each of the constituent phases. The isentropic bulk modulus of the dense phase at the reference state is B_t^η. From prior work,[5,6,20,53] its value is close to that of water: $B_t^\eta = 2.3$ GPa. The isentropic bulk modulus of air under the ideal gas model is $B_a^\eta = \Gamma B_a^T = \Gamma p_{a0}$, with $\Gamma = 1.4$ the ratio of specific heat at constant pressure to that at constant volume of air.

The Grüneisen parameter is obtained from the thermodynamic identity[67,70]

$$g_0 = A_0 \bar{B}_0^T / c_0, \tag{57}$$

where A_0 and c_0 are found from Eq. 55. The effective isothermal bulk modulus $\bar{B}_0^T$ at the reference state is defined by regime similarly to Eq. 56:

$$\bar{B}_0^T = \begin{cases} B_0^T & \text{(open-cell model)}, \\ \left[\frac{v_t}{B_t^T} + \frac{1-v_t}{p_{a0}} \right]^{-1} & \text{(closed-cell model)}. \end{cases} \tag{58}$$

Summarizing, thermoelastic coefficients A_0, c_0, and g_0 always depend on v_t and p_{a0}. The composite isothermal bulk modulus $\bar{B}_0^T$ depends on v_t and p_{a0} under the closed-cell assumption, but it is independent of phase volume fraction and airway pressure in the open-cell model, where it becomes the constant B_0^T. The composite isentropic bulk modulus $\bar{B}_0^\eta$ always depends on v_t and p_{a0}, though its dependence in the open-cell model arises only indirectly via g_0 and A_0. Surface tension coefficient K_0, shear moduli μ_0 and G_0 and their ambient pressure derivatives, and higher-order elastic coefficients c_1, c_2, and c_3 are all assumed to be constants, irrespective of tissue volume fraction and internal airway pressure.

2.5 Viscoelasticity

The viscoelastic response is the same for closed- and open-cell models because air in the closed-cell model is treated as an inviscid compressible fluid (e.g., ideal gas) that does not contribute to dynamic viscosity. Two independent parameters (material constants) enter the specific theory for the lung: the dimensionless dynamic bulk modulus amplification factor β_1 and the relaxation time t_1. Dynamic viscous stiffness is $\mu_1 = \beta_1 B_0^T$ and dynamic viscosity is $\nu_1 = \mu_1 t_1$. Thermal and entropic effects are omitted in the configurational free and internal energies associated with viscoelasticity, in part because moderate temperature variations do not strongly affect stiffness or hysteresis,[73] and because sufficient data do not exist for the lung to

enable parameterization of a dynamic viscosity function $\mu_1(T)$ or $\mu_1(\eta)$.

The specific relaxation internal energy U_0^1 is

$$U_0^1(\boldsymbol{\epsilon}) = \frac{1}{2}\mu_1|\boldsymbol{\epsilon}|^2 = \frac{1}{2}\mu_1\left[(\ln J)^2 + \epsilon_1^2 + \epsilon_2^2 + \epsilon_3^2 + \alpha^2 + \beta^2 + \gamma^2\right]. \tag{59}$$

The total configurational internal energy is

$$\Upsilon_0[\boldsymbol{\epsilon}, \boldsymbol{\chi}^1] = \frac{1}{2}\mu_1\left[|\boldsymbol{\chi}^1|^2 - 2\boldsymbol{\epsilon}\cdot\boldsymbol{\chi}^1 + |\boldsymbol{\epsilon}|^2\right] = \frac{1}{2}\mu_1|\boldsymbol{\chi}^1 - \boldsymbol{\epsilon}|^2. \tag{60}$$

This is partitioned into dilatational, squeeze, and shear contributions:

$$\Upsilon_0 = \Upsilon_0^V + \Upsilon_0^\mu + \Upsilon_0^G; \tag{61}$$

$$\begin{aligned}
\Upsilon_0^V &= \frac{1}{2}\mu_1(\epsilon_0 - \chi_0^1)^2, \\
\Upsilon_0^\mu &= \frac{1}{2}\mu_1\sum_{i=1,2,3}(\epsilon_i - \chi_i^1)^2, \\
\Upsilon_0^G &= \frac{1}{2}\mu_1\sum_{i=4,5,6}(\epsilon_i - \chi_i^1)^2.
\end{aligned} \tag{62}$$

The viscous internal stress obeys $\boldsymbol{\zeta}^1 = -\partial_{\boldsymbol{\chi}^1}U_0 = -\partial_{\boldsymbol{\chi}^1}\Upsilon_0$. Its time evolution is given by

$$\dot{\boldsymbol{\zeta}}^1 + \frac{1}{t_1}\boldsymbol{\zeta}^1 = \mu_1\dot{\boldsymbol{\epsilon}}, \qquad \boldsymbol{\zeta}^1|_{t=0} = \boldsymbol{\zeta}_0^1 = \partial_{\boldsymbol{\epsilon}}\Psi_0^1\big|_{\boldsymbol{\epsilon},T \text{ at } t=0} = \mu_1\boldsymbol{\epsilon}_0. \tag{63}$$

A solution of Eq. 63 is given by the convolution integral

$$\boldsymbol{\zeta}^1(t) = \mu_1\boldsymbol{\epsilon}_0\exp\left(\frac{-t}{t_1}\right) + \mu_1\int_{0^+}^{t}\exp\left[\frac{-(t-s)}{t_1}\right]\left(\frac{\mathrm{d}}{\mathrm{d}s}\left[\boldsymbol{\epsilon}(s)\right]\right)\mathrm{d}s. \tag{64}$$

Internal strain $\boldsymbol{\chi}^1$ and its rate obey

$$\boldsymbol{\chi}^1 = \boldsymbol{\epsilon} - \frac{\boldsymbol{\zeta}^1}{\mu_1}, \qquad \dot{\boldsymbol{\chi}}^1 = \frac{\boldsymbol{\zeta}^1}{\nu_1}, \qquad (\nu_1 = \mu_1 t_1 = \beta_1 B_0^T t_1 > 0). \tag{65}$$

The squeeze terms in the internal strain vector sum to zero, in analogy with the volume-preserving property of squeeze strain attributes in Eq. 16: $\sum_{i=1,2,3}\chi_i^1 = 0$. The rate of dissipated energy is unconditionally nonnegative: $|\boldsymbol{\zeta}^1|^2/\nu_1 = \nu_1|\dot{\boldsymbol{\chi}}^1|^2 \geq$

0. At equilibrium as $t \to \infty$, the viscous internal stress vanishes and internal strain equals thermoelastic strain: $\boldsymbol{\chi}^1_\infty = \boldsymbol{\epsilon}$.

2.6 Damage

The internal state variable representative of deleterious processes that affect mechanical and/or biological functions is universally denoted by the internal state variable $D \in [0, 1]$. Degradation functions $\bar{f}(D)$ and $f(D)$ introduced in Eq. 47 are required, along with kinetic rules for how $D(\boldsymbol{X}, t)$ may change during the history of loading at a material point $\boldsymbol{X}$.

The thermodynamic driving force for damage in Eq. 43 is found in terms of thermoelastic strain, viscous internal strain, and entropy by equating partial derivatives of free and internal energies with respect to D:

$$\bar{F} = -\left.\frac{\partial \Psi}{\partial D}\right|_{\boldsymbol{\epsilon}, \boldsymbol{\chi}^\alpha, T} = -\left.\frac{\partial U}{\partial D}\right|_{\boldsymbol{\epsilon}, \boldsymbol{\chi}^\alpha, \eta}. \tag{66}$$

This derivation is analogous to that followed for obtaining stress components as partial strain derivatives of internal energy in Eq. 37.[48,49] The thermodynamic driving force for damage of Eq. 66 is then, from differentiation of Eq. 47,

$$\begin{aligned} \bar{F} &= -\left[\frac{\mathrm{d}\bar{f}}{\mathrm{d}D} U_0^V + \frac{\mathrm{d}f}{\mathrm{d}D}(U_0^\mu + U_0^G)\right] \\ &= -\bar{f}'\left[U_0^{V\infty} + \Upsilon_0^V\right] - f'\left[U_0^{\mu\infty} + \Upsilon_0^\mu + U_0^{G\infty} + \Upsilon_0^G\right]. \end{aligned} \tag{67}$$

A linear degradation function of classical damage mechanics is used for f, here in the context of internal energy rather than free energy:

$$f(D) = 1 - D, \qquad f' = \mathrm{d}f/\mathrm{d}D = -1. \tag{68}$$

This linear function is contrasted with quadratic functions used in phase field and other generalized continuum theories,[74–77] which are all admissible in the generic thermodynamic framework of recent publications.[48,49] The bulk degradation func-

tion $\bar{f}$ is

$$\bar{f}(D) = 1 - \bar{D}(D);$$
$$\bar{D}(D) = \begin{cases} D \cdot \left(1 - \frac{B_a^\eta}{\bar{B}_0^\eta}\right) = D \cdot \left(1 - \frac{\Gamma p_{a0}}{\bar{B}_0^\eta}\right) = D \cdot (1 - \bar{\gamma}) & \text{(closed-cell model)}, \\ D & \text{(open-cell model)}. \end{cases} \tag{69}$$

Denoted by $\bar{\gamma} \leq 1$ is the ratio of the bulk modulus of the gas phase to that of the composite material for the closed-cell theory. Accordingly, as $D \to 1$, $\bar{f} \to \bar{\gamma}$, and the bulk stiffness of the composite at null applied strain reduces to that of the air contained within: $\bar{B}_0^\eta \to B_{a0}^\eta = \Gamma p_{a0}$. From Eq. 69, the derivative of $\bar{f}$ with respect to damage is

$$\bar{f}'(D) = \begin{cases} \bar{\gamma} - 1 & \text{(closed-cell model)}, \\ -1 & \text{(open-cell model)}. \end{cases} \tag{70}$$

It follows from insertion of Eqs. 68, 69, and 70 into Eq. 66 that, in order to ensure that damage evolution is physically and thermodynamically irreversible,

$$\dot{D} \geq 0, \qquad \bar{F}\dot{D} = \bar{U}_0 \dot{D} \geq 0. \tag{71}$$

A conditional internal energy density per unit reference volume $\bar{U}_0 = \bar{F}$ is defined as

$$\bar{U}_0 = \begin{cases} (1 - \bar{\gamma}) U_0^V + U_0^\mu + U_0^G & \text{(closed-cell model)}, \\ U_0 & \text{(open-cell model)}. \end{cases} \tag{72}$$

Internal energy $\bar{U}_0$ of the undamaged material, with the bulk energy factored by $(1-\bar{\gamma})$ in the closed-cell case, is thermodynamically conjugate to the rate of damage growth in the dissipation product $\bar{F}\dot{D}$ entering total dissipation rate $\mathfrak{D}$ of Eq. 45.

A canonical constitutive assumption is that D, or its rate, should be driven by a conjugate thermodynamic force U_0 or $\bar{U}_0$. The following dimensionless transformation

of U_0 is defined for use subsequently as a driving force or indicator of damage:

$$Z(U_0, \nabla_0 U_0) = \begin{cases} \left[2 \left| \frac{U_0^{V\infty}}{B_0^\eta} + \frac{\Upsilon_0^V}{B_0^\eta} + \frac{U_0^{\mu\infty} + \Upsilon_0^\mu}{\mu_0} + \frac{U_0^{G\infty} + \Upsilon_0^G}{G_0} \right| \right]^{1/2} \cdot [1 + \omega(|\nabla_0 U_0|)] & (\text{if } \bar{U}_0 \geq 0), \\ 0 & (\text{if } \bar{U}_0 < 0). \end{cases} \tag{73}$$

The factor $1 + \omega$ appears only in the present internal energy-based model intended for moderate to high strain rates, most notably those involving wave propagation. Arguments of Z are indicated only implicitly by those in parenthesis on the left of Eq. 73. Rather, Z depends explicitly on partitioned and normalized contributions from U_0 and its reference gradient $\nabla_0 U_0$, where the latter only affects Z through ω.

The gradient augmentation function ω is defined as follows, with ω_D a dimensionless nonnegative scalar constant and l a length parameter later associated with alveolar diameter and used for normalization along with the open-cell bulk modulus B_0^η:

$$\omega = \omega_D \sqrt{\frac{l}{B_0^\eta}} |2\nabla_0 U_0|^{1/2} = \omega_D \sqrt{\frac{2l}{B_0^\eta}} \left[\frac{\partial U_0}{\partial X_K} \frac{\partial U_0}{\partial X_K} \right]^{1/4} \geq 0. \tag{74}$$

The function ω is included in the driving force Z to account for deleterious effects of pressure gradients on the lung when subjected to blast loading. Steep pressure rises have been experimentally and numerically associated with more severe injuries than those incurred by gradual loading to similar overall stress and strain magnitudes.[4,8,11] According to Eq. 74, the driving force for damage kinetics Z is amplified more strongly at fixed $\nabla_0 U$ when l increases, since the energy gradient in a local volume element of lung tissue is distributed over fewer (larger) alveoli. Also, Z is amplified more strongly when B_0^η decreases, since more compliant lung tissue will experience larger local strain fluctuations within the microstructure.

The damage evolution law makes use of the maximum value of instantaneous driving force Z defined in Eq. 73 over the time history of deformation at a given material point $\boldsymbol{X}$:

$$Z_m(\boldsymbol{X}, t) = \max_{s \in (-\infty, t]} Z(\boldsymbol{X}, s). \tag{75}$$

Damage then obeys the following conditional equations, where Z_m accounts for

normalized internal energy and its material gradient:

$$D(\boldsymbol{X},t)=\begin{cases}\exp\left[\frac{\alpha_D\{Z_m(\boldsymbol{X},t)-Z_0\}}{Z_0}\right]-1 & (\text{if } \frac{Z_m}{Z_0}\in\left[1,1+\frac{\ln 2}{\alpha_D}\right]),\\ 0 & (\text{if } \frac{Z_m}{Z_0}<1),\\ 1 & (\text{if } \frac{Z_m}{Z_0}>1+\frac{\ln 2}{\alpha_D}).\end{cases} \tag{76}$$

Parameters $Z_0 > 0$ and $\alpha_D \geq 0$ denote, respectively, the threshold for damage initiation and the factor for the rate of damage accumulation. The material time derivative of Eq. 76 provides the kinetic equation for damage growth:

$$\dot{D}=\begin{cases}\frac{\alpha_D}{Z_0}(1+D)\frac{\mathrm{d}Z_m}{\mathrm{d}t} & (\text{if } \frac{Z_m}{Z_0}\in\left[1,1+\frac{\ln 2}{\alpha_D}\right]),\\ 0 & (\text{otherwise}).\end{cases} \tag{77}$$

Since Z_m can only remain constant or increase with time via its definition in Eq. 75, and because $\alpha_D \geq 0$ and $Z_0 > 0$, damage is irreversible: $\dot{D} \geq 0$. Furthermore, $\dot{Z}_m > 0$ only in the domain $\bar{U}_0 \geq 0$ according to the definition of Z in Eq. 73. Therefore, $\bar{U}_0\dot{D} = \bar{F}\dot{D} \geq 0$, ensuring positive dissipation from damage kinetics according to Eq. 71. This damage model requires only three calibrated parameters: Z_0, α_D, and ω_D.

The magnitude of damage state variable $D \in [0, 1]$ is lended the following progressive physical interpretations in the context of trauma mechanisms:

- $D \in (0, 0.1]$: injury threshold slightly exceeded, permeability changes, edema, near-negligible stiffness change;
- $D \in [0.1, 0.3]$: hemorrhage, contusion, minor tearing of membranes and vessel walls, small but detectable stiffness change;
- $D \in [0.3, 1.0]$: major tearing of membranes and vessel walls, failure of septal chords, atelectasis (collapse) in compression or rupture in tension, large to catastrophic stiffness loss.

See Fig. 1 for a graphical depiction of these approximate regimes of severity in relation to exponential growth of D as prescribed by the kinetic model in Eq. 76. Since D is a local field variable, its value pertains to element-level phenomena in the context of FE simulations, at length scales on the order of microns to millimeters.

For example, tearing, collapse, and rupture would correspond to trauma at the level of a representative ensemble of alveoli within the parenchyma, and not the entire organ. Rather, the value of D integrated or averaged over a finite region of the lung could be considered as a metric for overall severity of injury to the organ. Obviously, larger magnitudes of D witnessed over larger volumes of tissue should correspond to more traumatic injury and more compromised biological function of the entire lung.

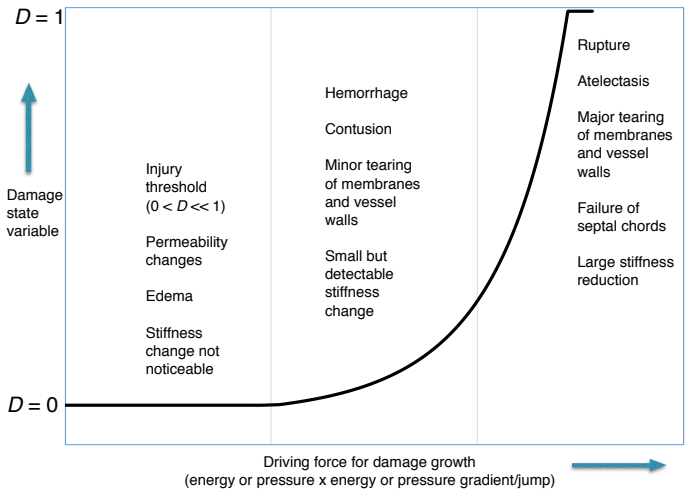

Fig. 1 Physical processes related to injury and microstructure degradation occurring in lung tissue in conjunction with evolution of damage state variable D. Exponential growth versus driving force is consistent with kinetic law in Eq. 76.

Mechanical degradation commensurate with local tearing or rupture will occur concurrently in a dynamic loading event, at time scales on the order of milliseconds. Permeability increases, edema, contusion, and other biological changes require substantially longer times to manifest and become observable.[1,9,13,19,28,39,40] In terms of representation of these longer-time mechanisms, a value of D, which is nondecreasing by construction, recorded real-time in a dynamic event is understood to correlate with biological changes that will be observed in the material later in time.[18]

2.7 Stresses, Entropy, and Temperature

Derivatives of the internal energy function—consisting of terms for thermoelasticity, viscoelasticity, and damage—produce stress components and temperature ac-

cording to Eq. 37. Equilibrium internal energy U_0^∞ of Eq. 50, thermal energy u of Eq. 53, configurational energy of Υ_0 of Eq. 60, and damage degradation functions f of Eq. 68 and $\bar{f}$ of Eq. 69 are substituted into Eq. 47 to yield the following total internal energy function:

$$
\begin{aligned}
&U(\xi_1,\xi_2,\xi_3,\eta,\boldsymbol{\chi}^1,D)\\
&=(1-\bar{D})\left[\frac{1}{2}\frac{\bar{B}_0^\eta}{c_1}\{\exp[c_1(\xi_1)^2]-1\}+K_0\xi_1-g_0T_0\eta\xi_1+\frac{1}{2}\mu_1(\epsilon_0-\chi_0^1)^2\right]\\
&\quad+(1-D)\left[3\frac{\mu_0}{c_2}\{\exp[c_2\xi_2]-1\}\left(1-\frac{B_0^T}{\mu_0}\mu_0'\xi_1\right)\right]\\
&\quad+(1-D)\left[\frac{1}{2}\frac{G_0}{c_3}\{\exp[c_3\xi_3]-1\}\left(1-\frac{B_0^T}{G_0}G_0'\xi_1\right)\right]\\
&\quad+(1-D)\left[\frac{1}{2}\sum_{i=1}^{6}\mu_1(\epsilon_i-\chi_i^1)^2\right]+T_0\eta\left(1+\frac{1}{2}\frac{\eta}{c_0}\right).
\end{aligned}
\tag{78}
$$

Stress components conjugate to strain attributes obtained from Eqs. 37 and 78 are

$$
\begin{aligned}
\hat{\tau}_0&=(1-\bar{D})\{\bar{B}_0^\eta\left[\epsilon_0\exp(c_1\xi_1^2)\right]-g_0T_0\eta+B_0^T\beta_1(\epsilon_0-\chi_0^1)+K_0\}\\
&\qquad-(1-D)B_0^T\{3\mu_0'\xi_2+\tfrac{1}{2}G_0'\xi_3\},\\
\hat{\tau}_1&=6(1-D)\mu_0\left[\epsilon_1\exp(c_2\xi_2)(1-\{B_0^T/\mu_0\}\mu_0'\xi_1)+\beta_2(\epsilon_1-\chi_1^1)\right],\\
\hat{\tau}_2&=6(1-D)\mu_0\left[\epsilon_2\exp(c_2\xi_2)(1-\{B_0^T/\mu_0\}\mu_0'\xi_1)+\beta_2(\epsilon_2-\chi_2^1)\right],\\
\hat{\tau}_3&=6(1-D)\mu_0\left[\epsilon_3\exp(c_2\xi_2)(1-\{B_0^T/\mu_0\}\mu_0'\xi_1)+\beta_2(\epsilon_3-\chi_3^1)\right],\\
\hat{\tau}_4&=(1-D)G_0\left[\epsilon_4\exp(c_3\xi_3)(1-\{B_0^T/G_0\}G_0'\xi_1)+\beta_3(\epsilon_4-\chi_4^1)\right],\\
\hat{\tau}_5&=(1-D)G_0\left[\epsilon_5\exp(c_3\xi_3)(1-\{B_0^T/G_0\}G_0'\xi_1)+\beta_3(\epsilon_5-\chi_5^1)\right],\\
\hat{\tau}_6&=(1-D)G_0\left[\epsilon_6\exp(c_3\xi_3)(1-\{B_0^T/G_0\}G_0'\xi_1)+\beta_3(\epsilon_6-\chi_6^1)\right].
\end{aligned}
\tag{79}
$$

Three dimensionless ratios β_i $(i=1,2,3)$ for viscoelastic stiffening are

$$
\beta_1=\frac{\mu_1}{B_0^T},\qquad \beta_2=\frac{\mu_1}{6\mu_0}=\beta_1\frac{B_0^T}{6\mu_0},\qquad \beta_3=\frac{\mu_1}{G_0}=\beta_1\frac{B_0^T}{G_0}.
\tag{80}
$$

Only one parameter out of the set of four parameters μ_1 and β_i $(i=1,2,3)$ is independent. Instantaneous dynamic moduli at the reference state ($\xi_i=0$, $D=0$, $\boldsymbol{\chi}^1=\mathbf{0}$) are

$$
\bar{B}_d^\eta=\bar{B}_0^\eta+\beta_1B_0^T,\qquad \mu_d=\mu_0\cdot(1+\beta_2),\qquad G_d=G_0\cdot(1+\beta_3).
\tag{81}
$$

Cauchy stress $\boldsymbol{\sigma}$ can be obtained from $\hat{\tau}_i$ and Eqs. 36 and 17 when $\boldsymbol{F} = \boldsymbol{QR}$ is imposed at a material point. Verification is straightforward that the constraints $\sum_{i=1,2,3} \hat{\tau}_i = 0$ of Eqs. 21 and 32 are obeyed automatically.

Absolute temperature is determined from Eq. 37 as follows, recalling that Υ_0, U_0^μ, and U_0^G do not depend on η:

$$T = \frac{\partial}{\partial \eta}\left[\bar{f} U_0^{V\infty} + u\right] = T_0 \left[1 - (1-\bar{D}) g_0 \ln J + \frac{\eta}{c_0}\right]. \tag{82}$$

Accordingly, temperature tends to increase with decreasing volume and increasing entropy. Total dissipation in Eq. 45 is

$$\mathfrak{D} = \beta_1 B_0^T t_1 \left[(1-\bar{D})(\dot{\chi}_0^1)^2 + (1-D)\sum_{i=1}^{6}(\dot{\chi}_i^1)^2\right] + \bar{U}_0 \dot{D} \geq 0, \tag{83}$$

where the (in)equality is verified with dynamic viscosity $\nu_1 = \beta_1 B_0^T t_1 > 0$. An energy balance similar to Eq. 44 in the form of a temperature rate equation still holds, but this is not needed since Eq. 82 can be used to obtain the temperature when deformation and entropy are known. For continuous processes, the latter is obtained from integration of the differential equation in Eq. 45:

$$\dot{\eta} = \frac{1}{T}\left[\mathfrak{D} - \nabla_0 \cdot \boldsymbol{q} + r\right], \tag{84}$$

where heat flux $\boldsymbol{q}$ and heat source r vanish by definition only for adiabatic problems.

2.8 Energy Gradient to Rate Transformation

The original form of the damage kinetic model[6,20] requires the material gradient of internal energy $\nabla_0 U_0$ that enters the amplification function ω of Eq. 74 within the driving force Z of Eq. 73. This gradient is not readily calculable in the context of standard explicit finite elements. Its magnitude can be estimated,[18] however, as follows for a planar longitudinal shock wave propagating at Lagrangian velocity v_s:

$$|\nabla_0 U_0| = \left|\frac{\partial U_0}{\partial X}\right| = \left|\frac{\partial U_0}{\partial t}\left(\frac{\mathrm{D}X}{\mathrm{D}t}\right)^{-1}\right| = \frac{|\dot{U}_0|}{v_s} \approx \frac{|\dot{U}_0|}{c_L} \to \frac{\langle \dot{U}_0 \rangle}{c_L}. \tag{85}$$

Angled brackets parse positive values: $\langle(\cdot)\rangle = \frac{1}{2}[|(\cdot)| + (\cdot)]$. To avoid potentially nonphysical damage amplification during rapid unloading, $|\dot{U}_0| \to \langle \dot{U}_0 \rangle$ is used

such that only positive energy rates are applied to ω. This prescription impedes further damage accumulation during viscoelastic unloading (e.g., as in the decaying half of a triangular pulse when stress and strain rate have opposite signs). Cavity formation is not excluded; for example, the energy rate will be positive if conjugate stress and strain rate components are of the same sign, as occurs in expansion under tensile pressure. Likewise, collapse commensurate with volume reduction under compressive pressure is captured.

The approximation $\upsilon_s \approx c_L$ is further invoked in Eq. 85, most accurate in the weak shock regime, where c_L is the longitudinal wave speed. The longitudinal and shear wave speeds are found in the absence of initial damage as, respectively,[6,20]

$$c_L = \sqrt{\frac{\bar{B}_d^\eta + \frac{4}{3}\mu_d}{\rho_0}}, \qquad c_S = \sqrt{\frac{G_d}{\rho_0}}. \tag{86}$$

According to the kinetic model of Eq. 76 and experimental evidence,[8,11,78] likelihood and severity of injury increase with increasing $|\nabla_0 U_0|$. According to Eq. 73, Eq. 76, and Eq. 85, for a fixed amount of energy density U_0 supplied by a wave pulse at a fixed wave speed $\upsilon_s \geq c_L$, injury severity increases with increasing rate of deposition $\dot{U}_0$. With this approximation, the injury metric used herein becomes similar to the criterion of a recent study on blast lung in sheep,[13] where the maximum product of strain and strain rate over the time history of deformation was correlated with local lung contusion. The ratio of material time derivative of pressure to wave speed was suggested as a contributor to lung injury similarly elsewhere.[78]

The transformation from gradient to rate form in Eq. 85 is intended for the solution of problems wherein damage and injury are induced by stress waves from dynamic impact or blast loading. Whether Eq. 85 should be used for homogeneous high-strain-rate loading remains to be explored. Its use in such instances, with the same value of amplification factor ω_D used for shock loading, might be expected to over-predict mechanical stiffness reduction and loss of biological function.

2.9 Fully Intact Stiffness Model

The reduction in mechanical stiffness, commensurate with local injury afforded by the theory of prior subsections and previous works,[6,18,20] though physically plausible, has not been verified by experimental data. A simplified version of the theory, newly presented herein, treats internal state variable D only as an indicator of decremented biological function, without thermodynamic or mechanical implications. According to this alternative perspective, physical interpretations for ranges of $D \in [0, 1]$ correlate with local biological injury mechanisms listed in Section 2.6 and Fig. 1, but not with local stiffness degradation.

Mathematically, the original theory of prior subsections is transformed as follows for the fully intact stiffness model. Free and internal energy densities in Eq. 27 simplify to

$$\Psi = \Psi(\boldsymbol{\epsilon}, T, \boldsymbol{\chi}^\alpha), \qquad U = U(\boldsymbol{\epsilon}, \eta, \boldsymbol{\chi}^\alpha). \tag{87}$$

The conjugate thermodynamic force to D vanishes: $\bar{F} = -\partial U/\partial D = 0$ with obvious ramifications to the temperature rate in Eq. 44 and dissipation in Eq. 45. In the internal energy function of Eq. 47, $\bar{f} = f = 1 \Rightarrow U = U_0$. Concurrently, $f' = 0$ in Eq. 68 and $\bar{f}' = 0$ in Eq. 70.

The kinetic laws for damage evolution, with origins still physically motivated from continuum damage mechanics, are unchanged in the fully intact stiffness model. Specifically, Eq. 76 still applies, where the same driving force Z_m of Eq. 75 is used. Energy gradient augmentation via ω defined in Eq. 74 likewise is still applicable, as is the transformation to rate augmentation described in Section 2.8.

The damage variable D still evolves with thermomechanical loading, but coupling with the thermomechanical response is one-way (i.e., mechanics affect D but D does not affect mechanics). Since $\bar{F} = 0$, the dissipation $\bar{F}\dot{D} \to 0$ for any $\dot{D} \geq 0$. In the final expressions for internal energy density of Eq. 78, stress components of Eq. 79, and temperature of Eq. 82, the fully intact stiffness model corresponds to the *symbolic* transformations $\bar{D} \to D \to 0$. Likewise, $\bar{U}_0 \to 0$ in Eq. 83.

3. Numerical Implementation

The constitutive model of Section 2 is implemented as a user material subroutine in the LS−DYNA software,[44] version R12.0 (2020). The implementation has presently only been verified with three-dimensional solid elements, and only with explicit dynamic solution of the momentum balance and integration of the equations of motion.[79] The full deformation gradient tensor $\boldsymbol{F}$ is stored at each integration point with initial coordinates $\boldsymbol{X}$, along with components of the Cauchy stress tensor $\boldsymbol{\sigma}$, the elastic energy density U_0, temperature T, entropy η, and the local damage-injury internal state variable D. All of these variables are updated with each time step. The pivoting algorithm of Freed et al.[58,65] is invoked point-wise for unique indexing of the Cartesian coordinate basis vectors in the context of the upper triangular decomposition.

For time scales pertinent to impact and blast loading, heat conduction is presumed negligible and adiabatic conditions (i.e., $\boldsymbol{q} = \boldsymbol{0}$, $r = 0$) are recommended. Regardless, temperature increases are small and do not significantly affect predicted stresses or damage in the lung tissue for the problems solved in prior works[5,18] or presumably in problems solved later in this report over comparable time durations.

At the dynamic rates pertinent for the present loading modes, and for solution time scales on the order of $0.1t_1$ or less, viscous relaxation does not significantly affect predicted stresses or damage as shown in prior works.[6,20] Thereby, numerical calculations are streamlined via use of dynamic elasticity coefficients rather than incrementally updating the viscoelastic kinetic equations in Section 2.5. As such, $\boldsymbol{\chi}^1 = \boldsymbol{0}$ and $\boldsymbol{\zeta}^1(t) = \mu_1 \boldsymbol{\epsilon}(t)$. Viscoelasticity is still very important, however, since effective dynamic coefficients are often stiffer than their quasi-static counterparts, as evidenced by values of β_i ($i = 1, 2, 3$) in Eq. 80 on the order of unity.[18]

The closed-cell model of the bulk modulus in Section 2.4 and the consistent closed-cell model for damage evolution in Section 2.6 are likewise used in the implementation commensurate with high-rate loading. Stress attributes of Eq. 79 become the

following for instantaneous viscoelastic response:

$$
\begin{aligned}
\hat{\tau}_0 &= (1-\bar{D})\{\bar{B}_0^{\eta}\left[\epsilon_0 \exp(c_1\xi_1^2)\right] - g_0 T_0 \eta + B_0^T \beta_1 \epsilon_0 + K_0\} \\
&\quad - (1-D) B_0^T \{3\mu_0' \xi_2 + \tfrac{1}{2} G_0' \xi_3\}, \\
\hat{\tau}_1 &= 6(1-D)\mu_0 \left[\epsilon_1 \exp(c_2\xi_2)(1 - \{B_0^T/\mu_0\}\mu_0'\xi_1) + \beta_2 \epsilon_1\right], \\
\hat{\tau}_2 &= 6(1-D)\mu_0 \left[\epsilon_2 \exp(c_2\xi_2)(1 - \{B_0^T/\mu_0\}\mu_0'\xi_1) + \beta_2 \epsilon_2\right], \\
\hat{\tau}_3 &= 6(1-D)\mu_0 \left[\epsilon_3 \exp(c_2\xi_2)(1 - \{B_0^T/\mu_0\}\mu_0'\xi_1) + \beta_2 \epsilon_3\right], \\
\hat{\tau}_4 &= (1-D) G_0 \left[\epsilon_4 \exp(c_3\xi_3)(1 - \{B_0^T/G_0\}G_0'\xi_1) + \beta_3 \epsilon_4\right], \\
\hat{\tau}_5 &= (1-D) G_0 \left[\epsilon_5 \exp(c_3\xi_3)(1 - \{B_0^T/G_0\}G_0'\xi_1) + \beta_3 \epsilon_5\right], \\
\hat{\tau}_6 &= (1-D) G_0 \left[\epsilon_6 \exp(c_3\xi_3)(1 - \{B_0^T/G_0\}G_0'\xi_1) + \beta_3 \epsilon_6\right].
\end{aligned}
\tag{88}
$$

Several approaches for installing a user material subroutine are documented in Appendix A of Volume I of the `LS-DYNA` user manual.[44] The procedure implemented in the present research builds a custom *mppdyna* executable for MPI (message passing interface) software platforms. For version R12.0, only one `LS-DYNA` source file need be edited: `dyn21umats.f`. The material subroutine for the lung constitutive model is implemented as particular subroutine `umat50` within this file. The `umat50` subroutine is incorporated in the `dyn21umats.f` file according to the algorithms described next. Afterwards, the source code is compiled to create the aforementioned *mppdyna* executable for parallel processing.

Let subscripts $(\cdot)_n$ and $(\cdot)_{n+1}$ denote quantities corresponding to solution times t_n and t_{n+1} for an explicit dynamic analysis, where the current time step is $\Delta t = t_{n+1} - t_n$. Quantities without such subscripts are constant over the time step. The user material subroutine receives the deformation gradient at the end of the step, $\boldsymbol{F}_{n+1}$, and the applicable state variables at the beginning of the step including damage, temperature, entropy, and internal elastic energy $(D_n, T_n, \eta_n, U_{0|n})$. The internal variable $\boldsymbol{\chi}^1$ is not needed under the instantaneous viscosity approximation described previously. Algorithms are coded in the subroutine according to the following sequence, where numbered equations correspond to Section 2 of this report:

1. Pass in material property array, history variable array, control parameters.

2. Assign material properties (note $\mu_0 = G_0$ and $\mu_0' = G_0'$; see Section 4): $\bar{B}_{\eta}^d, G_d, c_1, c_2, c_3, G_0', K_0, \rho_0, B_0^T, \beta_1, c_0, g_0, Z_0, \alpha_D, \omega_D, l$.

3. Assign initial (i.e., body) temperature $T_0 = 310$ K.
4. If $Z_0 < 0$, instantiate intact stiffness option (Section 2.9) and $Z_0 \rightarrow |Z_0|$.
5. Calculate $\mu_1, \bar{B}_0^{\eta}, G_0, \beta_2, \beta_3, \bar{\gamma}$.
6. Assign history variables at the beginning of the step: $D_n, \eta_n, T_n, U_{0|n}, Z_{m|n}$.
7. Assign deformation gradient at the end of the step, $\boldsymbol{F}_{n+1}$.
8. Calculate orthonormal pivoting matrix $\mathbf{P}$ using published algorithm.[58,65]
9. Pivot deformation gradient $\boldsymbol{F}_{n+1} \rightarrow \mathbf{P}^{\mathrm{T}}\boldsymbol{F}_{n+1}\mathbf{P}$.
10. Calculate $\boldsymbol{C}_{n+1}$ and $\boldsymbol{R}_{n+1}$ using Eqs. 9 and 10.
11. Calculate $a, b, c, \alpha, \beta, \gamma$ at t_{n+1} using Eq. 11, and $J_{n+1} = (abc)_{n+1}$.
12. Calculate $\boldsymbol{\epsilon}_{n+1}$ using Eq. 15.
13. Calculate $\boldsymbol{R}_{n+1}^{-1}$ using Eq. 12, followed by $\boldsymbol{Q}_{n+1} = \boldsymbol{F}_{n+1}\boldsymbol{R}_{n+1}^{-1}$.
14. Calculate $\xi_{i|n+1}$ $(i = 1, 2, 3)$ of Eq. 49.
15. If $B_0^T G_0' \xi_{1|n+1}/G_0 \geq 1$, restrict tangent shear modulus to a minimum of 0.
16. Calculate the non-degraded internal elastic energy density $U_{0|n+1}$ of Eq. 48.
17. Calculate the time rate of energy density using a backward difference: $\dot{U}_0 = (U_{0|n+1} - U_{0|n})/\Delta t$.
18. Calculate the driving force term $\bar{U}_0$ using Eq. 72 for the closed-cell model.
19. Calculate wave speed c_L via Eq. 86, with tangent moduli degraded by a factor of $1 - D_n$ (shear) or $1 - \bar{D}_n$ (bulk) unless the fully intact stiffness model is used.
20. Calculate the estimate of elastic energy gradient $|\nabla_0 U_0|$ from Eq. 85.
21. Calculate the gradient amplification factor ω from Eq. 74.
22. Calculate the instantaneous damage driving force Z_{n+1} using Eq. 73.
23. Invoke Eq. 75: if $Z_{n+1} > Z_{m|n}$, then $Z_{m|n+1} = Z_{n+1}$; else $Z_{m|n+1} = Z_{m|n}$.

24. Update the local damage-injury state variable using Eq. 76.

25. Calculate $\bar{D}_{n+1}$ using Eq. 69.

26. Integrate entropy density $\eta_{n+1} = \eta_n + \dot{\eta}\Delta t$ using Eq. 84 for $\dot{\eta}$ with T_n and $\dot{D} = (D_{n+1} - D_n)/\Delta t$.

27. Calculate temperature T_{n+1} using Eq. 82.

28. Calculate stress attributes $\hat{\tau}_{i|n+1}$ $(i = 0, \ldots, 6)$ using Eq. 88 verbatim for the standard model or $\bar{D} = D = 0$ in Eq. 88 for the fully intact stiffness model.

29. Calculate the rotated stress tensor $\boldsymbol{s}_{n+1}$ using Eq. 36.

30. Calculate the Cauchy stress tensor $\boldsymbol{\sigma}_{n+1}$ in the re-indexed coordinate frame using Eq. 17: $\boldsymbol{\sigma}_{n+1} = J_{n+1}^{-1}\boldsymbol{Q}_{n+1}\boldsymbol{s}_{n+1}\boldsymbol{Q}_{n+1}^{\mathrm{T}}$.

31. Pivot the stress tensor back to the original coordinate system: $\boldsymbol{\sigma}_{n+1} \rightarrow \mathbf{P}\boldsymbol{\sigma}_{n+1}\mathbf{P}^{\mathrm{T}}$.

32. Return the Cauchy stress components in the `sig` array:
    $\texttt{sig}(1) = \sigma_{11|n+1}$,
    $\texttt{sig}(2) = \sigma_{22|n+1}$,
    $\texttt{sig}(3) = \sigma_{33|n+1}$,
    $\texttt{sig}(4) = \sigma_{12|n+1}$,
    $\texttt{sig}(5) = \sigma_{23|n+1}$,
    $\texttt{sig}(6) = \sigma_{13|n+1}$.

33. Return the history variables in the `hsv` array:
    $\texttt{hsv}(1) = D_{n+1}$,
    $\texttt{hsv}(2) = \eta_{n+1}$,
    $\texttt{hsv}(3) = T_{n+1} - T_0$,
    $\texttt{hsv}(4) = U_{0|n+1}$,
    $\texttt{hsv}(5) = Z_{m|n+1}$,
    $\texttt{hsv}(6) = \omega_{n+1}$.

34. Return the absolute temperature and damage-injury variable:
    `temp` = T_{n+1},
    `epsp` = D_{n+1},
    where the latter overwrites "effective plastic strain" to be conveniently visualized in third-party post-processing software.

4. Parameters for the Human Lung

The parameters in Table 1 for animal lung were calibrated to experimental data on dog and several other species, as discussed in the Introduction. All calibrations were reported in prior works[5,6,20] with the exception of ω_D that was obtained more recently[18] under the energy gradient-to-rate transformation of Section 2.8 for use in dynamic FE simulations.

The present objective is estimation of a suitable set of corresponding parameters for human lung. Finite-strain elasticity data on human lung tissue are limited.[41,43] Further complicating parameterization is the noted stiffening of the human lung with certain diseases and aging.[42] Mass density of human lung in a reference or resting state (at least partially inflated, not collapsed) could range from 0.1 to 0.6 g/cc (1 cc = 1 cm^3) according to prior works,[8,28,47,80] with density decreasing and transpulmonary pressure increasing upon inspiration. The value of ρ_0 for canine lung used in prior works, 0.337 g/cc, is thus credible for human lung as well, with the same dense tissue fraction υ_t.

The mean alveolar diameter l for humans[81] is around three times that prescribed for dogs. From comparison of biaxial extension data on dog and human lung tissue, isothermal, open-cell, second-order elastic constants $B_0^T \approx B_0^\eta$ and $G_0 = \mu_0$ of human are also roughly three times those of dog.[41] To effect the same mass density at the reference state, surface tension K_0 should thus also be three times greater in humans than dogs. The aforementioned changes in elastic properties and normalization length are effected as follows, where $(\cdot)_h$ and $(\cdot)_c$ denote respective human and canine values:

$$(B_0^T)_h \approx 3(B_0^T)_c, \qquad (G_0)_h \approx 3(G_0)_c, \qquad (K_0)_h \approx 3(K_0)_c, \qquad l_h \approx 3l_c. \tag{89}$$

Specific heat per unit volume and thermal expansion are assumed the same among species, consistent with equal υ_t. The closed-cell isentropic modulus $\bar{B}_0^\eta$ is likewise the same from Eq. 56. With these assumptions, g_0 is unchanged by Eq. 57. Insufficient data exist to support new values of c_1, c_2, G_0', β_1, Z_0, and α_D for human lung; hence, canine values are assumed to carry over for humans. The value of nonlinear shear elastic constant c_3 is updated for human lung following analysis of dynamic simple shear in Section 2.1.

In prior research with animal lung properties,[18] comparison of numerical predictions of the present lung model with data[28,40] for edema induced by pressure wave loading (i.e., shock tube compression) and projectile impact suggested a plausible range of $0.5 \leq \omega_D \leq 30$ for the energy gradient/rate amplification to local damage and injury. Since, as noted previously,[18] further data and analysis are required to obtain a precise value of ω_D, the same range is explored parametrically later in calculations of this report pertinent to human subjects. Notice from Eq. 74 that the ratio $\frac{\omega}{\omega_D}$ is unchanged when l and B_0^η are simultaneously multiplied by a factor of 3 as in Eq. 89. Thus, the same range of ω_D should be valid, as a first approximation, for both animals and humans.

Table 1 Suggested parameter values for animal[18,20] and human lung parenchyma

Property (units)	Animal	Human	Description
$\bar{B}_0^\eta$ (kPa)	213	213	closed-cell bulk modulus ($p_{a0} = 1$ atm)
B_0^T (kPa)	2.5	7.5	open-cell isothermal bulk modulus
G_0 (kPa)	1.0	3.0	shear modulus*
G_0'	-0.7	-0.7	pressure derivative of shear modulus**
c_1	3	3	nonlinear elastic bulk constant
c_2	10	10	nonlinear elastic squeeze constant
c_3	0.5	1	nonlinear elastic shear constant
K_0 (kPa)	0.2	0.6	reference surface tension in air
ρ_0 (g/cm^3)	0.337	0.337	lung mass density at $J = 1$
c_0 (kPa/K)	741	741	specific heat capacity ($p_{a0} = 1$ atm)
g_0	$4.91 \cdot 10^{-4}$	$4.91 \cdot 10^{-4}$	Grüneisen parameter ($p_{a0} = 1$ atm)
β_1	0.6	0.6	viscoelastic dynamic multiplier
Z_0	0.64	0.64	normalized injury threshold
α_D	0.0167	0.0167	rate-independent damage kinetics
ω_D	0.5–30	0.5–30	gradient/rate enhanced damage kinetics
l (μm)	60.1	180.3	mean alveolar diameter

$^*\mu_0 = G_0$
$^{**}\mu_0' = G_0'$

4.1 Simple Shear

Model predictions for adiabatic simple shear are compared with dynamic experimental data[36,43] in Fig. 2. The imposed homogeneous deformation gradient is

$$\boldsymbol{F}(t) = \mathbf{1} + \dot{\gamma} t \, \boldsymbol{e}_1 \otimes \boldsymbol{e}_2, \qquad \gamma(t) = \int_0^t \dot{\gamma} \mathrm{d}t, \tag{90}$$

where γ is the shear strain. The shear stress reported in Fig. 2 is $\tau = \sigma_{12}$. The complete analytical solution to this problem, including time-dependent viscoelastic

effects, was derived in a previous report.[20] Results therein verified that the predicted instantaneous viscoelastic response is nearly identical to the complete time-dependent viscoelastic response, where the latter is omitted herein.

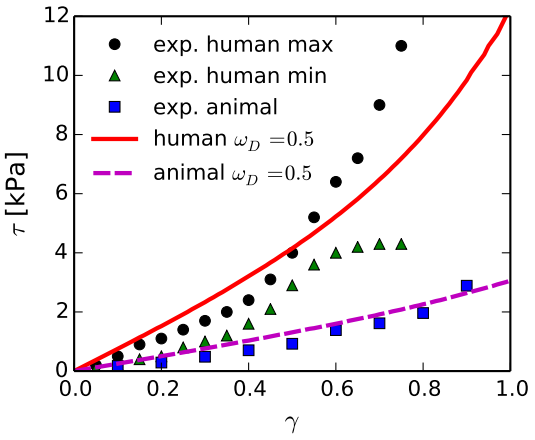

(a) shear stress $\omega_D = 0.5$

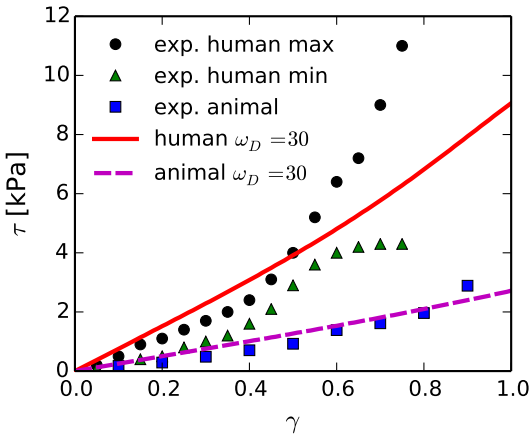

(b) shear stress $\omega_D = 30$

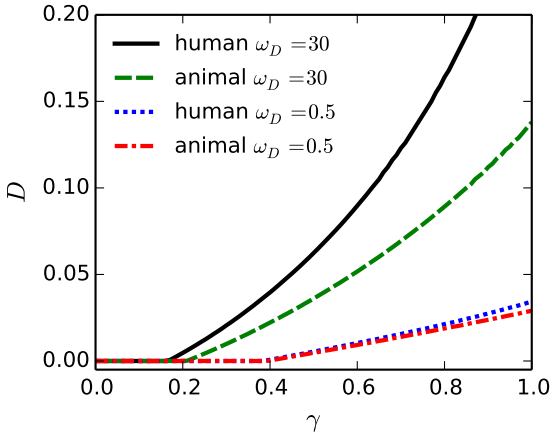

(c) damage-injury metric

Fig. 2 Model response in dynamic simple shear at $\dot{\gamma} = 1000$ s^{-1} compared to experimental data on porcine lung[36] tested at $\dot{\gamma} = 550$ s^{-1} and human lung[43] tested at $\dot{\gamma} = 1305$ s^{-1} and $\dot{\gamma} = 2300$ s^{-1}: a) shear stress τ versus simple shear strain γ for $\omega_D = 0.5$, b) shear stress τ versus simple shear strain γ for $\omega_D = 30$, and c) damage variable D versus shear γ

For the present calculations, the solutions are obtained from FE simulations in `LS-DYNA` with a single hexahedral element. Evolution of damage-injury variable D is time-dependent in the present calculations due to $\omega_D > 0$. The parameter c_3 is chosen for human lung such that reasonable agreement with experimental data[43] is attained. When ω_D is increased from 0.5 to 30, damage accumulates more severely,

and softening of the tangent shear modulus leads to lower stress levels at larger shear strains. Human lung is notably stiffer in simple shear as evidenced by results in Figs. 2a and 2b. For the same value of ω_D, damage accumulates more rapidly in human than animal lung, as seen in Fig. 2c.

4.2 Uniaxial Strain Compression

Model predictions for adiabatic uniaxial strain compression are reported in Figs. 3 and 4 for animal and human lung, respectively. The imposed spatially homogeneous deformation gradient is

$$\boldsymbol{F}(t) = \mathbf{1} - \dot{\varepsilon} t \, \boldsymbol{e}_1 \otimes \boldsymbol{e}_1, \qquad \varepsilon(t) = \int_0^t \dot{\varepsilon} \mathrm{d}t, \tag{91}$$

where $\varepsilon = 1 - \rho_0/\rho$ is the nominal strain. This loading protocol provides results nearly identical to those obtained for planar shock compression since the entropy rise from shock dissipation is very small for the material properties of the lung when $\varepsilon \leq 0.4$.[5,6,20] The analytical solution to the planar shock problem was derived in a prior report,[20] and the numerical solution procedure invoked here (again, `LS-DYNA` with a single hexahedral element) was described in more detail in a prior publication.[18] The longitudinal (i.e., axial stress), positive in compression, is $P = -\sigma_{11}$. The shear stress is defined as is typical in shock physics[5,67]: $\tau = \frac{1}{2}|\sigma_{11} - \sigma_{22}|$.

Compared in Figs. 3 and 4 are predictions for active stiffness degradation with $\omega_D = 0.5$ and $\omega_D = 30$, as well as predictions for the fully intact stiffness option of Section 2.9 with $\omega_D = 30$. Longitudinal stress P and damage D are very similar for animal and human lung, where agreement of the former is expected given the same value of closed-cell bulk modulus $\bar{B}_0^\eta$ for animals and humans prescribed in Table 1. Shear stress τ is significantly higher in humans than animals upon comparison of Figs. 3b and 4b, which is expected considering the larger prescribed value of G_0 for the human lung. When ω_D is increased from 0.5 to 30, damage accumulates more rapidly, and softening of the tangent bulk and shear moduli leads to lower stress levels (especially lower τ) at larger strains. Shear stress τ decreases with increasing ε at large compressions due to damage softening as well as negative pressure dependence $G_0' < 0$ (i.e., the tangent shear modulus increases [decreases] with increasing [decreasing] transpulmonary pressure[26,82]). Results in Figs. 3c and 4c show that for $\omega_D = 30$, the local damage-injury metric accrues almost as quickly when the fully intact, rather than the standard damage-softening, model is used.

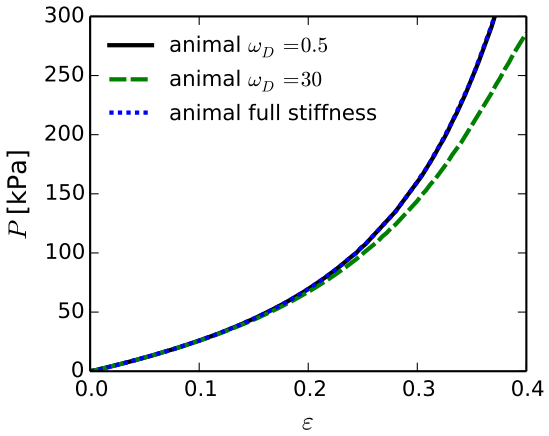

(a) normal stress animal

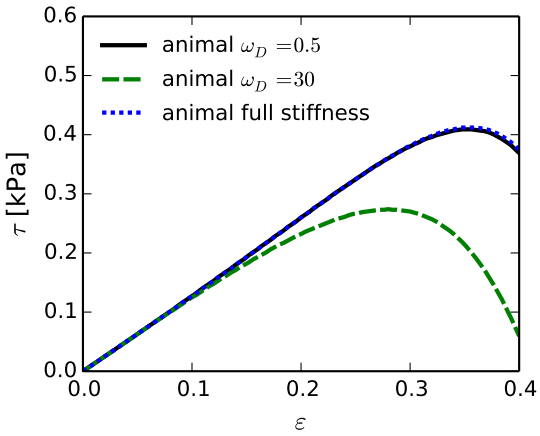

(b) shear stress animal

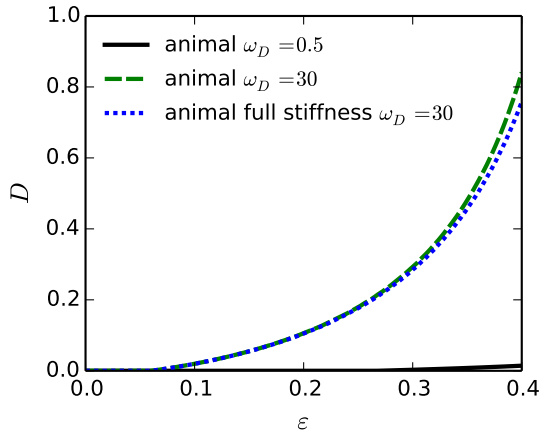

(c) damage-injury animal

Fig. 3 Model response for animal lung under adiabatic uniaxial strain compression at $\dot{\varepsilon} = 1000$ s^{-1}: a) longitudinal compressive stress P, b) shear stress τ, and c) damage variable D

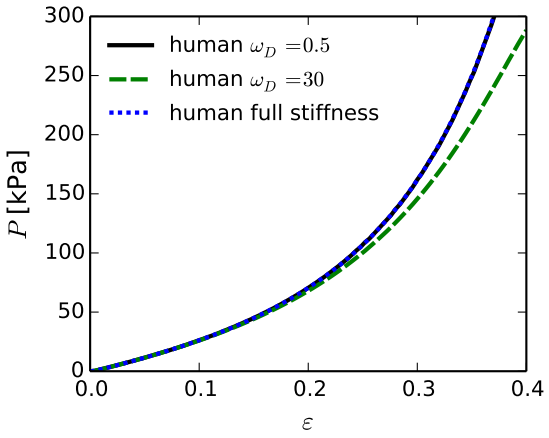

(a) normal stress human

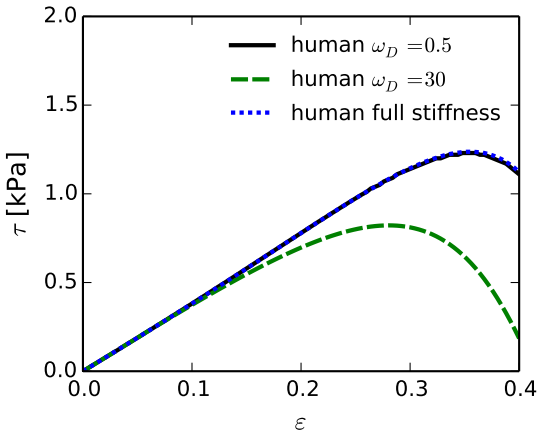

(b) shear stress human

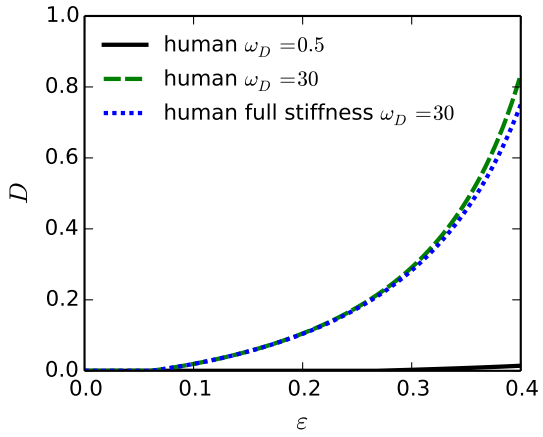

(c) damage-injury human

Fig. 4 Model response for human lung under adiabatic uniaxial strain compression at $\dot{\varepsilon} = 1000$ s^{-1}: a) axial compressive stress P, b) shear stress τ, and c) damage variable D

5. Human Torso Simulations

Simulations of impact of the human torso by a lightweight rod are reported. The LS−DYNA code is used, where the constitutive behavior of the lung is modeled according to the theory of Section 2, computer implementation of Section 3, and parameterization for human lung tissue of Section 4.

5.1 Advanced Total Body Model for LS−DYNA and Problem Setup

The FE model of the human torso and head implemented in LS−DYNA is known as the Advanced Total Body Model Version 2.5 (ATBM 2.5). The complete model consists of the FE mesh, constitutive behaviors, material properties, and simulation control parameters (e.g., contact and hourglass settings) for the human torso. Skin, muscle, connective tissue, the skeletal system, and internal organs, among other features, are all resolved explicitly. Library constitutive models available in LS−DYNA are used, consisting of linear elastic, nonlinear elastic, plastic, or viscoelastic materials depending on the particular biological constituent. The original ATBM 2.5 uses a low-density foam constitutive law[44] for the lungs. In the present work, this foam constitutive law is replaced with the nonlinear material model described in Sections 2, 3, and 4 of this report. A complete description of the other features (e.g., specific properties and parameters) of the ATBM 2.5 is outside the present scope. Various components of the geometry are visualized in Fig. 5.

The projectile[45] is a stiff impactor instrumented with a wired accelerometer. The striking end is covered by a 40-mm-diameter solid hemisphere made from a plastic material. This hemisphere, which inhibits perforation of the torso for high-impact velocities, is fastened to an aluminum housing that contains the accelerometer. The housing is connected to a long aluminum pushrod whose back end is fixed to a plastic cylinder that fits in the barrel of a pressurized launcher. The total mass of the FE representation of the projectile, created at the US Army Combat Capabilities Development Command Army Research Laboratory, is 72.3 g. The projectile strikes the right upper chest region in the present simulations.

Results of 10 simulations are reported, with parameters varied among simulations as listed in Table 2. The damage-injury kinetic factor ω_D is varied among values of 0.5 and 30, where the suggested minimum and maximum (see Table 1) are chosen based on prior simulations of shock tube and projectile impact loading of animal lung.[18]

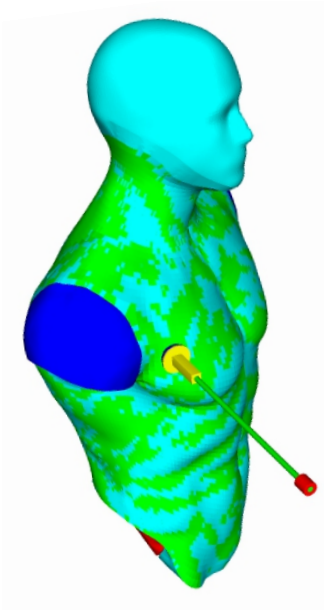

(a) external view with projectile

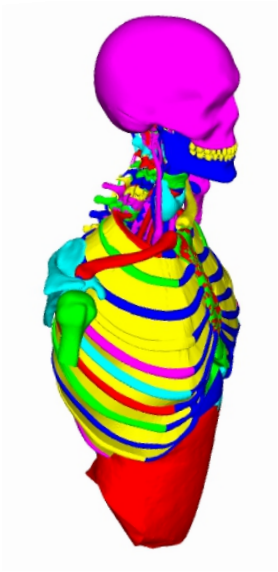

(b) skin & flesh removed

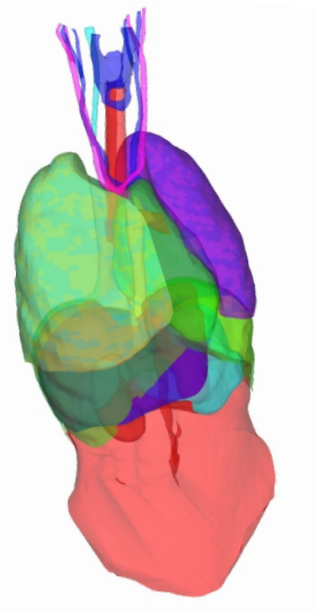

(c) internal organs

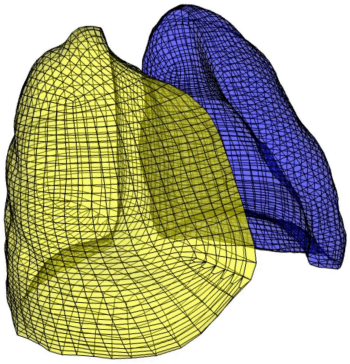

(d) lungs only

Fig. 5 Human ATBM 2.5: a) entire model including projectile, b) skull and torso with skin and flesh removed for visualization, c) torso with skin, flesh, and skeletal system removed for visualization, and d) lungs with hexahedral mesh

The rod impact velocity, denoted as v_I, is prescribed as 45 or 90 m/s. Corresponding kinetic energy (KE) of the rod is 73.2 or 292.8 J. Analogous experiments on live pigs[45] with $v_I \in [35, 95]$ m/s suggest that a threshold impact velocity of around 75 m/s exists, where lung injuries are usually observed for most velocities above, and are usually not observed for most velocities below. This threshold corresponds to a projectile kinetic energy of around 200 J. Injuries sustained by two human patients struck by nonlethal projectiles (rubber bullets) with kinetic energies around 200 J were evaluated in a different study.[83] In that work, one of the two patients suffered heart and lung contusion requiring hospitalization.

Finally, the initial mass density ρ_0 is varied among two values: 3.37 and 2.25 g/cc. The former value matches that of Table 1, and corresponds to the lung at rest. Upon inspiration, the volume increases and mass density decreases accordingly.[26,38] The latter value of 2.25 g/cc is intended to mimic the lung at maximum functional capacity. A precise correspondence between lung density and aspects of the respiratory cycle (e.g., tidal volume) is outside the scope of the present approximation. In reality, upon deep inhalation, tensile transpulmonary pressure p_{tp} would increase and compressive internal airway pressure p_{a0} would also increase. Tangent elastic coefficients would change due to the stretching of the tissue and the increased airway pressure, the latter inducing a near-negligible effect on $\bar{B}_0^\eta$ since the increase in p_{a0} is very small compared to 1 atm in Eq. 56. Experimental data on elasticity and wave velocities in sheep lung with closed trachea[27] showed a change in tangent bulk modulus on the order of only 10% for a nearly sixfold change in mass density with artificial inflation/deflation. The measured change in longitudinal wave speed was dominated by the mass density change, not the change in bulk and shear moduli. Changes in elastic properties commensurate with changes in ρ_0 are thus ignored as an approximation. Furthermore, the initial geometry of the lung is presumed the same for either density, so the more dense lung is more massive overall in the ATBM 2.5.

The first eight simulations in Table 2 invoke the usual theory of Section 2, where stiffness, internal energy, and entropy are affected by the damage-injury variable D in two-way coupling. Simulations 9 and 10, however, invoke the fully intact stiffness version of Section 2.9, whereby coupling of damage and mechanics is one-way.

Table 2 Parameters varied among `LS-DYNA` simulations of impact to the human torso

Simulation number	Impact vel. v_I (m/s)	Damage rate kinetics ω_D	Lung density ρ_0 (g/cm^3)
1	45	0.5	3.37
2	45	0.5	2.25
3	45	30	3.37
4	45	30	2.25
5	90	0.5	3.37
6	90	0.5	2.25
7	90	30.0	3.37
8	90	30.0	2.25
9	90	30.0*	3.37
10	90	30.0*	2.25

*Fully intact stiffness option (Section 2.9)

5.2 Results and Analysis

Displacement contours for the entire torso and head are visualized in Figs. 6 and 7 for respective simulations 3 and 7, corresponding to respective impact velocities of 45 and 90 m/s. In Cartesian coordinates, the displacement vector $\boldsymbol{u}$ and its magnitude u are

$$\boldsymbol{u}(\boldsymbol{X}, t) = \boldsymbol{x}(\boldsymbol{X}, t) - \boldsymbol{X}, \qquad u = |\boldsymbol{u} \cdot \boldsymbol{u}|^{1/2}. \tag{92}$$

In each depicted case, $\rho_0 = 3.37$ g/cc and $\omega_D = 30$, though such surface contours are insensitive to both mass density and the damage kinetic parameter. Displacement in the impacted zone is more severe for the higher projectile velocity. In both simulations, elastic recovery of the torso (i.e., recovery of the chest wall upon projectile rebound and decompression) takes place at later solution times (e.g., $t \geq 10$ ms).

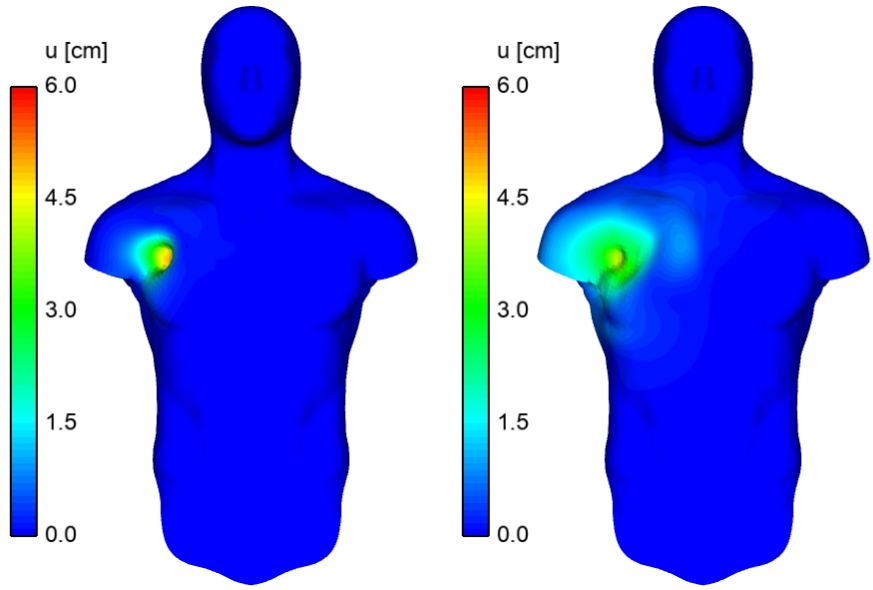

(a) 2 ms

(b) 5 ms

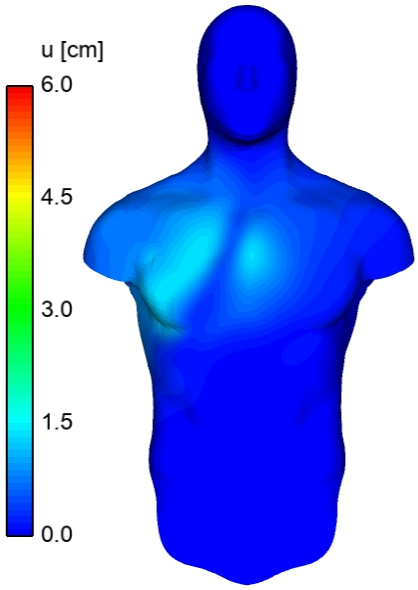

(c) 10 ms

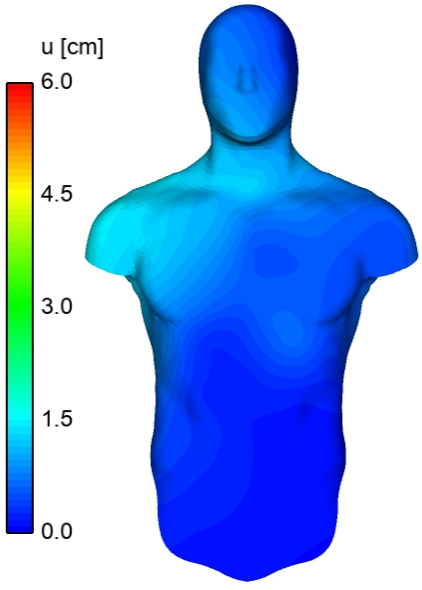

(d) 30 ms

Fig. 6 Surface displacement magnitude u, simulation 3 ($v_I = 45$ m/s): a) $t = 2$ ms, b) $t = 5$ ms, c) $t = 10$ ms, and d) $t = 30$ ms

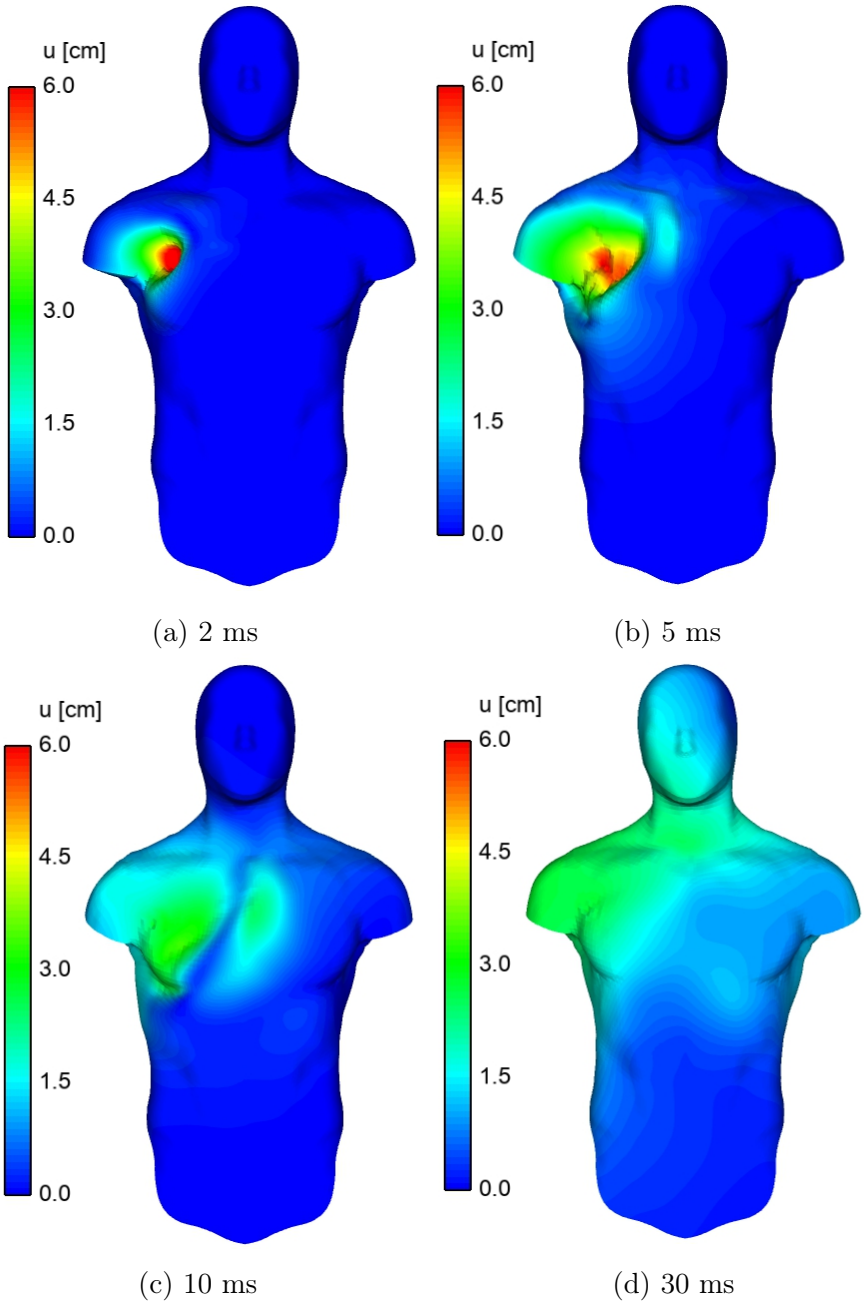

(a) 2 ms (b) 5 ms

(c) 10 ms (d) 30 ms

Fig. 7 Surface displacement magnitude u, simulation 7 ($v_I = 90$ m/s): a) $t = 2$ ms, b) $t = 5$ ms, c) $t = 10$ ms, and d) $t = 30$ ms

The subsequent seven figures (i.e., Figs. 8 through 14) show contours of local damage-injury field $D(\boldsymbol{X}, t)$ over surfaces of both lungs. All other components of the ATBM 2.5 mesh are removed for visualization, including the visceral pleural membranes addressed with a library viscoelasticity model. Simulation numbers refer to those of Table 2.

Results in Fig. 8 correspond to simulation 1, where the contour range is $D \in [0, 0.2]$ since damage magnitudes are low. For this low impact velocity (45 m/s) and low value of $\omega_D = 0.5$, negligible injury is predicted. Deformation of the right lung is large at $t = 5$ ms, but the organ elastically recovers its original shape by $t = 30$ ms.

Results in Fig. 9 correspond to simulation 3, where now the contour range is set to $D \in [0, 1]$ since damage magnitudes can attain unity locally. For this low impact velocity (45 m/s) and high value of $\omega_D = 30$, moderate injury is predicted. Deformation of the right lung is large at $t = 5$ ms, but the organ elastically recovers its original shape by $t = 39$ ms. Even though the tangent shear modulus is degraded in local regions where D is relatively large, the damaged material retains enough elasticity to return to its original shape upon unloading. Injury is confined to the right lung; the surface of the left lung is unscathed.

Contours of $D \in [0, 0.2]$ for simulation 5 are shown in Fig. 10. The impact velocity is high at 90 m/s, but the damage kinetic parameter $\omega_D = 0.5$ is low. Local injury is modest, with values $D > 0.2$ evident at a few hot spots on the surface of the right lung. Similarly, heterogeneous local injury patterns, with corresponding surface hot spots, were observed when a "strain product" criterion was used in FE simulations to correlate lung injury in sheep subjected to blast loading.[13] These hot spots are likely attributed to stress wave interactions leading to localized strain energy density and localized high energy rates, as speculated by Fung et al.[39] No injury is observed in the left lung in Fig. 10. Deformation of the right lung is severe, but it does elastically recover its shape by $t = 30$ ms.

Contours of $D \in [0, 1]$ are shown in Fig. 11 for simulation 7. The impact velocity is high at 90 m/s, as is the damage kinetic parameter $\omega_D = 30$. Local injury is severe, with values $D \approx 1$ over a significant area of the right lung surface for $t \geq 10$ ms. Internal elements experience similarly large local values of D. Mild injury is also observed in the left lung for $t \geq 10$ ms. Deformation and deterioration of the elastic properties of the right lung are so severe that shape recovery is unsuccessful

at $t = 30$ ms, as witnessed by crimping of the tissue at the lower left in Fig. 11d. Lung deformation up through the instance of maximum deflection is not apparently sensitive to ω_D, but elastic recovery is.

Aforementioned results in Figs. 8–11 considered only the denser lung material with $\rho_0 = 3.37$ g/cc, corresponding physically to a fully relaxed or partially inflated condition. Results in Figs. 12 and 13 compare injury contours at $t = 5$ ms for lungs at this density as well as a reduced density of $\rho_0 = 2.25$ g/cc corresponding to full inspiration. Also compared are results for two prescribed values of ω_D of 0.5 and 30.

Shown in Fig. 12 are contours of D for simulations 1 through 4, with an impact velocity of 45 m/s. Comparing part (a) with part (b), and part (c) with part (d), effects of lung density are very small, with slightly more surface damage observed for the higher density organ. Comparing part (a) with part (c), and part (b) with part (d), a drastic increase in D is observed when ω_D is increased from 0.5 to 30. However, the deformed shape of the lung at $t = 5$ ms does not change appreciably when ω_D is increased.

Similar conclusions are drawn from the high-velocity impact cases in Fig. 13: lung density ρ_0 has a small influence on D and the deformed shape of the lung *prior to elastic recovery*, while ω_D has a large effect on the evolution of D. The present results contrast findings in prior work[18] that predicted more severe lung damage with decreasing ρ_0 under pressure wave loading mimicking that from a shock tube. Those simulations[18] considered a rectangular block of bare lung tissue. The present simulations consider geometrically realistic lungs encased in viscoelastic pleura whose confinement might mitigate effects of initial density changes.

Finally, contours of D shown in Fig. 14 demonstrate effects of prescription of the fully intact stiffness model of Section 2.9 invoked in simulations 9 and 10, as opposed to the degraded model invoked in simulations 1 through 8. Impact velocity is $v_I = 90$ m/s, and the damage rate amplification is $\omega_D = 30$. Results show that use of the fully intact stiffness model versus the standard (i.e., degraded) stiffness model has nearly negligible influence on D contours at $t = 5$ ms. Deformed shapes are also very similar for all four cases depicted in Fig. 14.

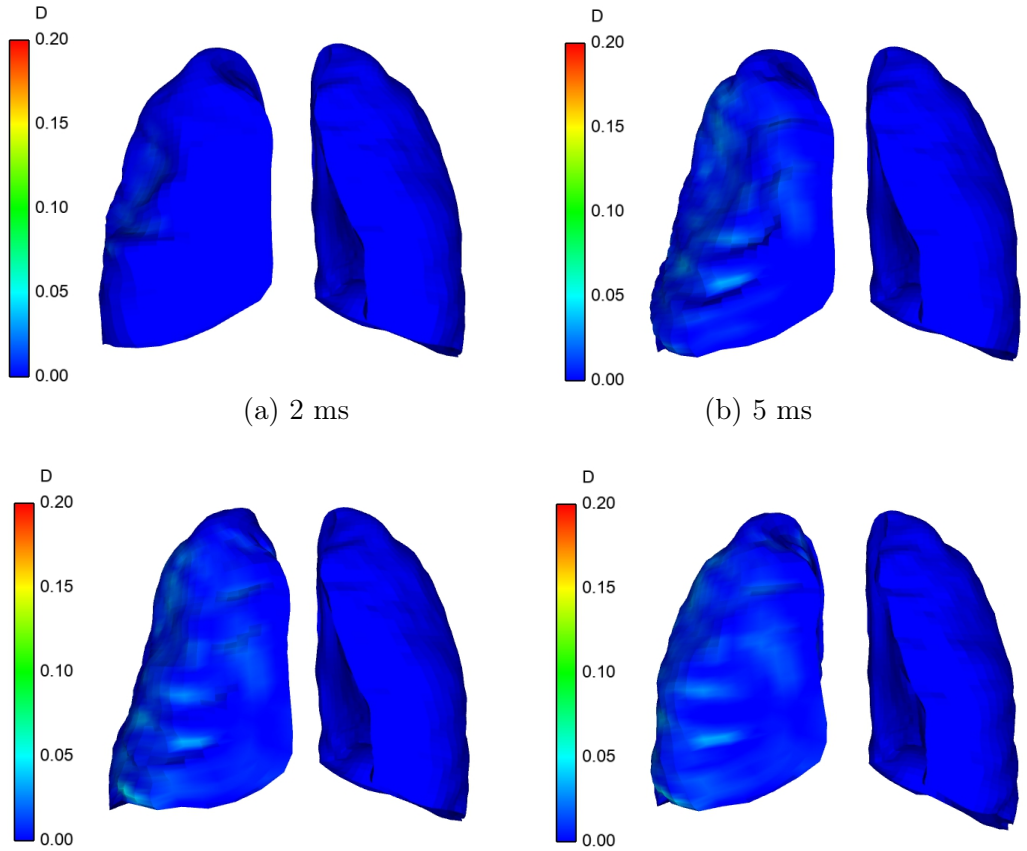

Fig. 8 Lung damage-injury variable D, simulation 1 ($v_I = 45$ m/s, $\omega_D = 0.5$): a) $t = 2$ ms, b) $t = 5$ ms, c) $t = 10$ ms, and d) $t = 30$ ms

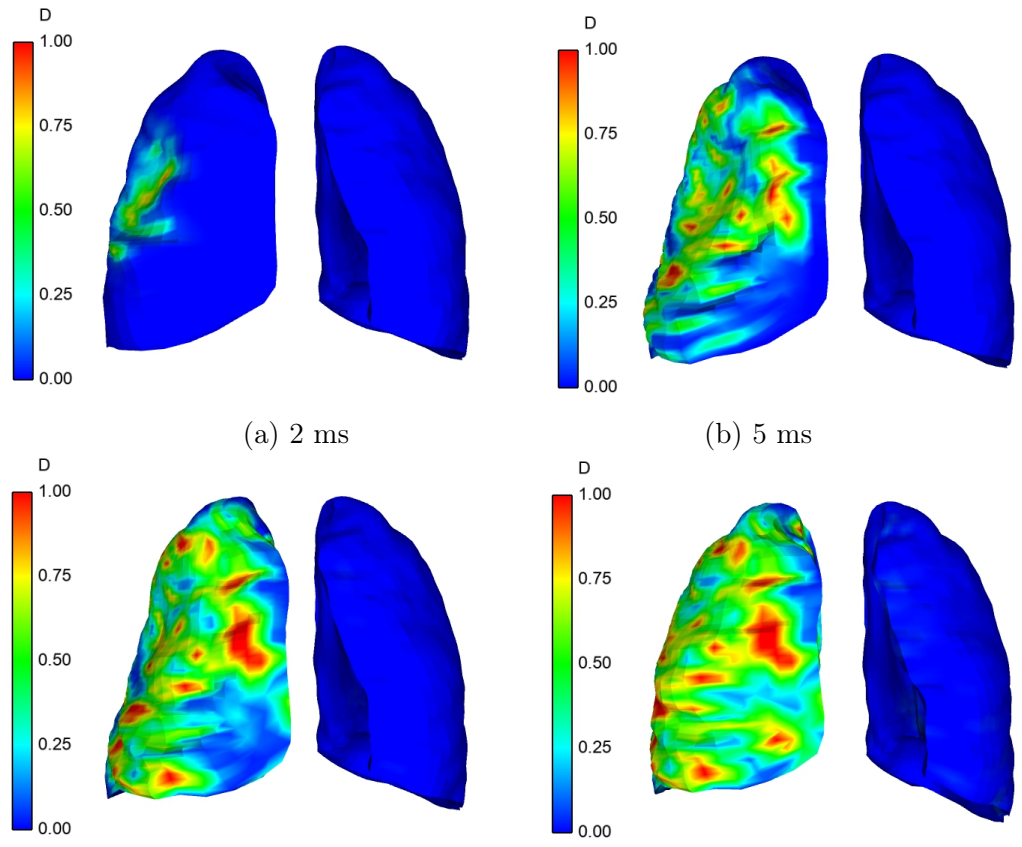

(a) 2 ms (b) 5 ms

(c) 10 ms (d) 39 ms

Fig. 9 Lung damage-injury variable D, simulation 3 ($v_I = 45$ m/s, $\omega_D = 30$): a) $t = 2$ ms, b) $t = 5$ ms, c) $t = 10$ ms, and d) $t = 39$ ms

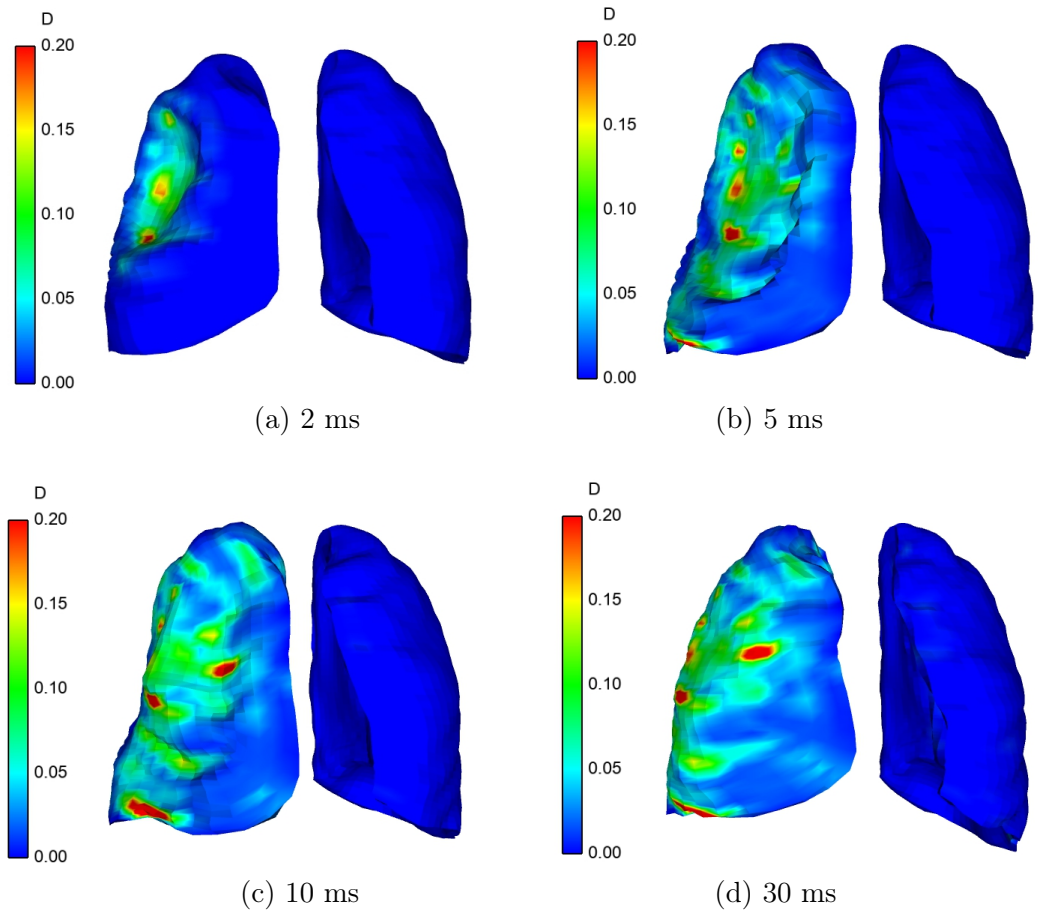

Fig. 10 Lung damage-injury variable D, simulation 5 ($v_I = 90$ m/s, $\omega_D = 0.5$): a) $t = 2$ ms, b) $t = 5$ ms, c) $t = 10$ ms, and d) $t = 30$ ms

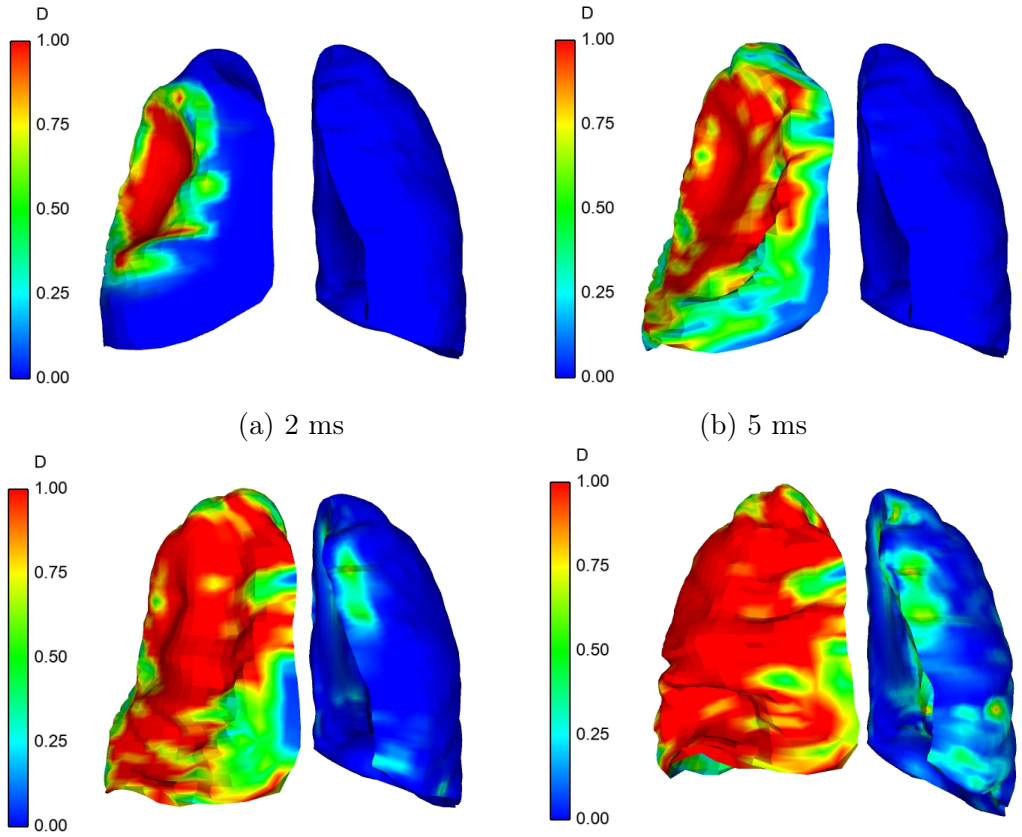

(a) 2 ms (b) 5 ms

(c) 10 ms (d) 30 ms

Fig. 11 Lung damage-injury variable D, simulation 7 ($\upsilon_I = 90$ m/s, $\omega_D = 30$): a) $t = 2$ ms, b) $t = 5$ ms, c) $t = 10$ ms, and d) $t = 30$ ms

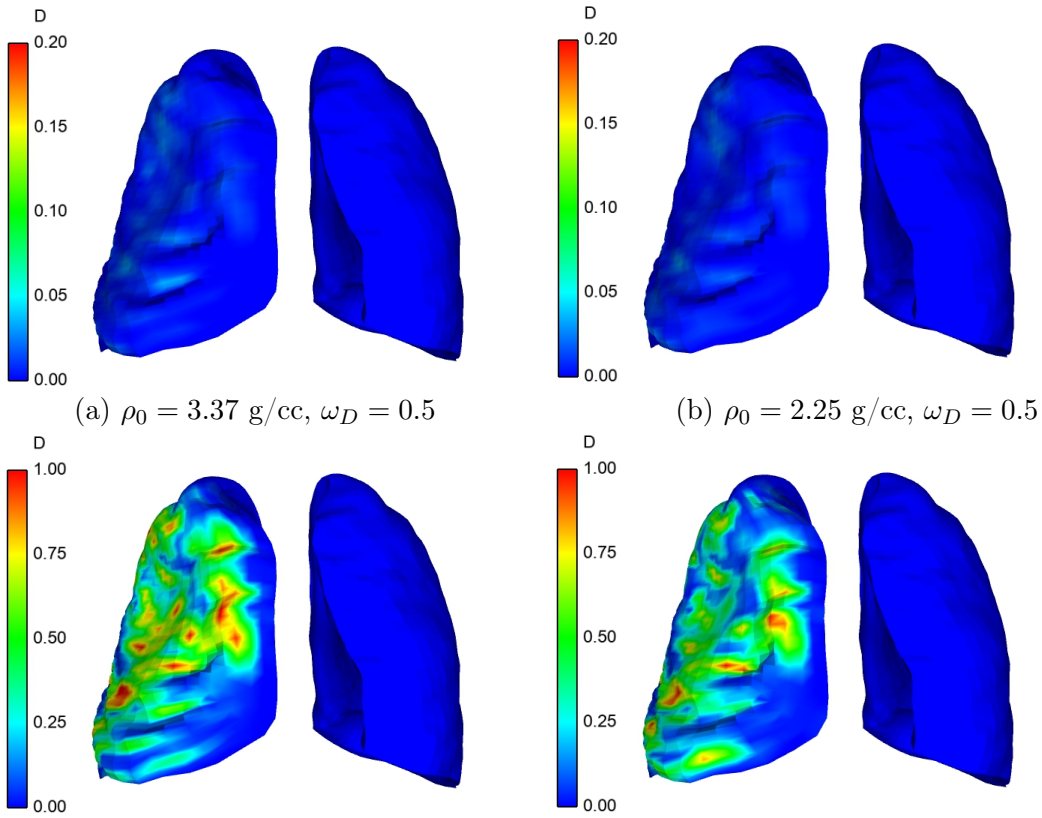

(a) $\rho_0 = 3.37$ g/cc, $\omega_D = 0.5$ (b) $\rho_0 = 2.25$ g/cc, $\omega_D = 0.5$

(c) $\rho_0 = 3.37$ g/cc, $\omega_D = 30$ (d) $\rho_0 = 2.25$ g/cc, $\omega_D = 30$

Fig. 12 Lung damage-injury variable D at $t = 5$ ms, $v_I = 45$ m/s: a) simulation 1, b) simulation 2, c) simulation 3, and d) simulation 4

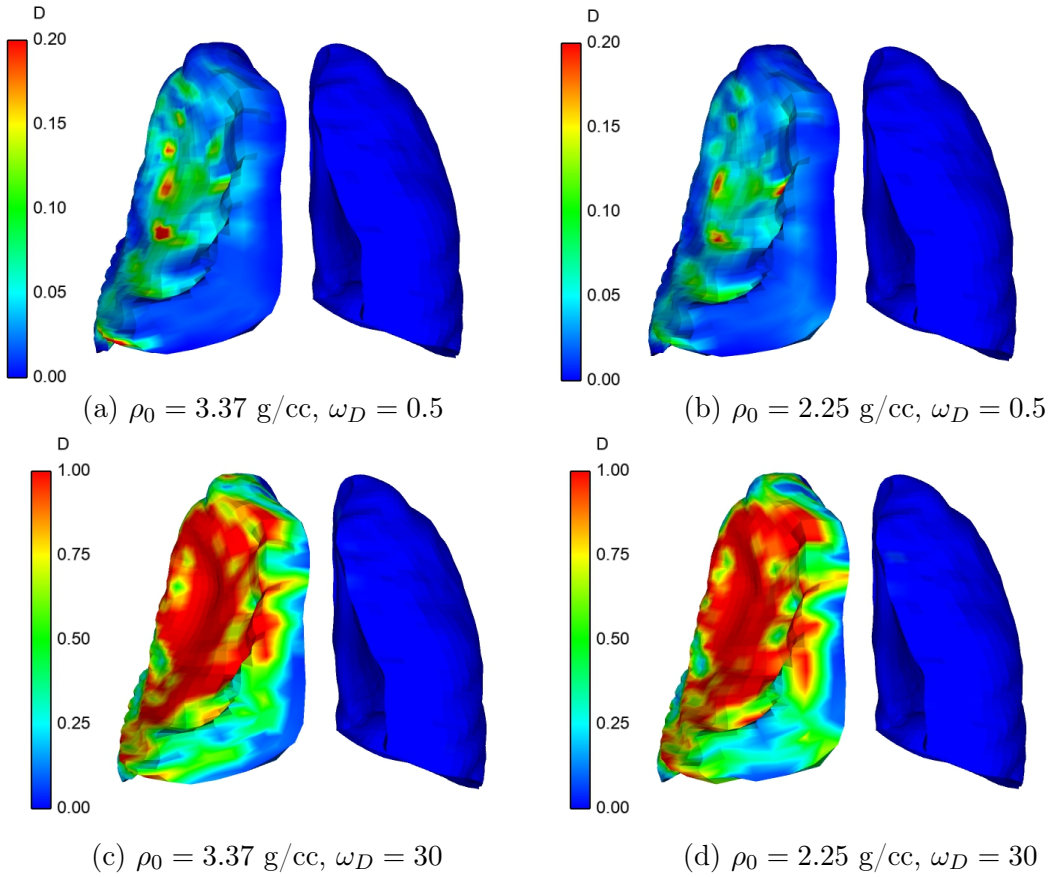

(a) $\rho_0 = 3.37$ g/cc, $\omega_D = 0.5$ (b) $\rho_0 = 2.25$ g/cc, $\omega_D = 0.5$

(c) $\rho_0 = 3.37$ g/cc, $\omega_D = 30$ (d) $\rho_0 = 2.25$ g/cc, $\omega_D = 30$

Fig. 13 Lung damage-injury variable D at $t = 5$ ms, $v_I = 90$ m/s: a) simulation 5, b) simulation 6, c) simulation 7, and d) simulation 8

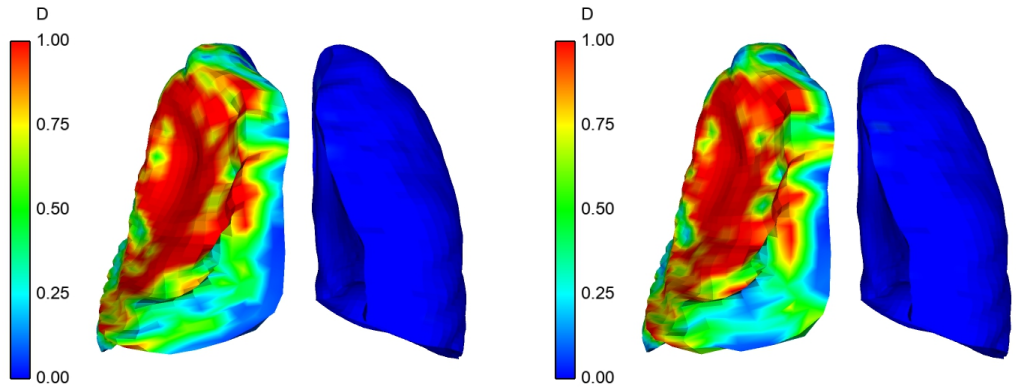

(a) $\rho_0 = 3.37$ g/cc, degraded

(b) $\rho_0 = 2.25$ g/cc, degraded

(c) $\rho_0 = 3.37$ g/cc, fully stiff

(d) $\rho_0 = 2.25$ g/cc, fully stiff

Fig. 14 Lung damage-injury variable D at $t = 5$ ms, $\omega_D = 30$, and $v_I = 90$ m/s: a) simulation 7, b) simulation 8, c) simulation 9, and d) simulation 10

A novel candidate global lung injury metric[18] is the maximum over the time history $t \in [0, t_f]$ of the volume-averaged local damage parameter D:

$$D_{V|max} = \max_{t\in[0,t_f]} D_V(t), \qquad D_V(t) = \frac{1}{V_0}\int_{V_0} D(\boldsymbol{X}, t)\, \mathrm{d}V_0(\boldsymbol{X}), \tag{93}$$

where V_0 is the initial lung volume and t_f is the final termination time, or a cut-off time, of a given analysis. Since $D(\boldsymbol{X}, t)$ cannot decrease with increasing t at any fixed point $\boldsymbol{X}$, and since each referential volume element $\mathrm{d}V_0$ is constant in time, it follows that $D_{V|max} = D_V(t)\,\forall\, t = t_f$ for the kinetic model of Section 2 for $D(\boldsymbol{X}, t)$. In other words, since local damage is irreversible, the referentially integrated value of $D_V(t)$ at any instant is identical to $D_{V|max}$ up to that instant.

Results in Fig. 15 show effects of impact velocity v_I, lung density ρ_0, and damage kinetic factor ω_D on $D_V(t)$. Limitations in post-processing capabilities required that $D_V(t)$ be estimated via a spatial volume integral over $V(t)$ rather than a reference volume average over V_0, where V_0 is taken as the sum of the initial volumes of both lungs, and $V(t)$ is the sum of current volumes of both lungs at time t. Regardless, $D_V(t)$ is nearly monotonically increasing, and its value at t nearly coincides with $D_{V|max}$ up to that time instant. Any transient decreases in D_V reported in Fig. 15 are numerical artifacts of spatial volume averaging. For impact at 45 m/s, D_V is negligible when $\omega_D = 0.5$ and attains a plateau of $D_{V|max} \approx 0.26 - 0.29$ for $\omega_D = 30$, with the upper limit associated with the higher density lung. For impact at 90 m/s, D_V is small but nonnegligible when $\omega_D = 0.5$, with a plateau of $D_{V|max} \approx 0.03$ for $\omega_D = 0.5$. When $\omega_D = 30$, average damage is more severe, with $D_{V|max} \approx 0.53$. Results for v_I in Fig. 15c demonstrate that use of the full stiffness option of Section 2.9 does not noticeably affect $D_V(t)$. Differences incurred by different prescriptions of ρ_0 are greater than those incurred by election of the full stiffness option. Comparison of results in parts (a) and (b) demonstrates the strong influence of the energy rate amplification factor on predicted magnitudes of the integrated injury metric D_V.

Two other global criteria used elsewhere[46,47] for various thoracic injuries are compared in the context of the current numerical simulations: the compression criterion C_{max} and the viscous criterion VC_{max}. Consider dynamic blunt impact or blast loading normal to the anterior chest wall. Denote by $u_1(t)$ and $v_1(t)$ the displacement and velocity, respectively, of the skin at the front of the thorax where impact

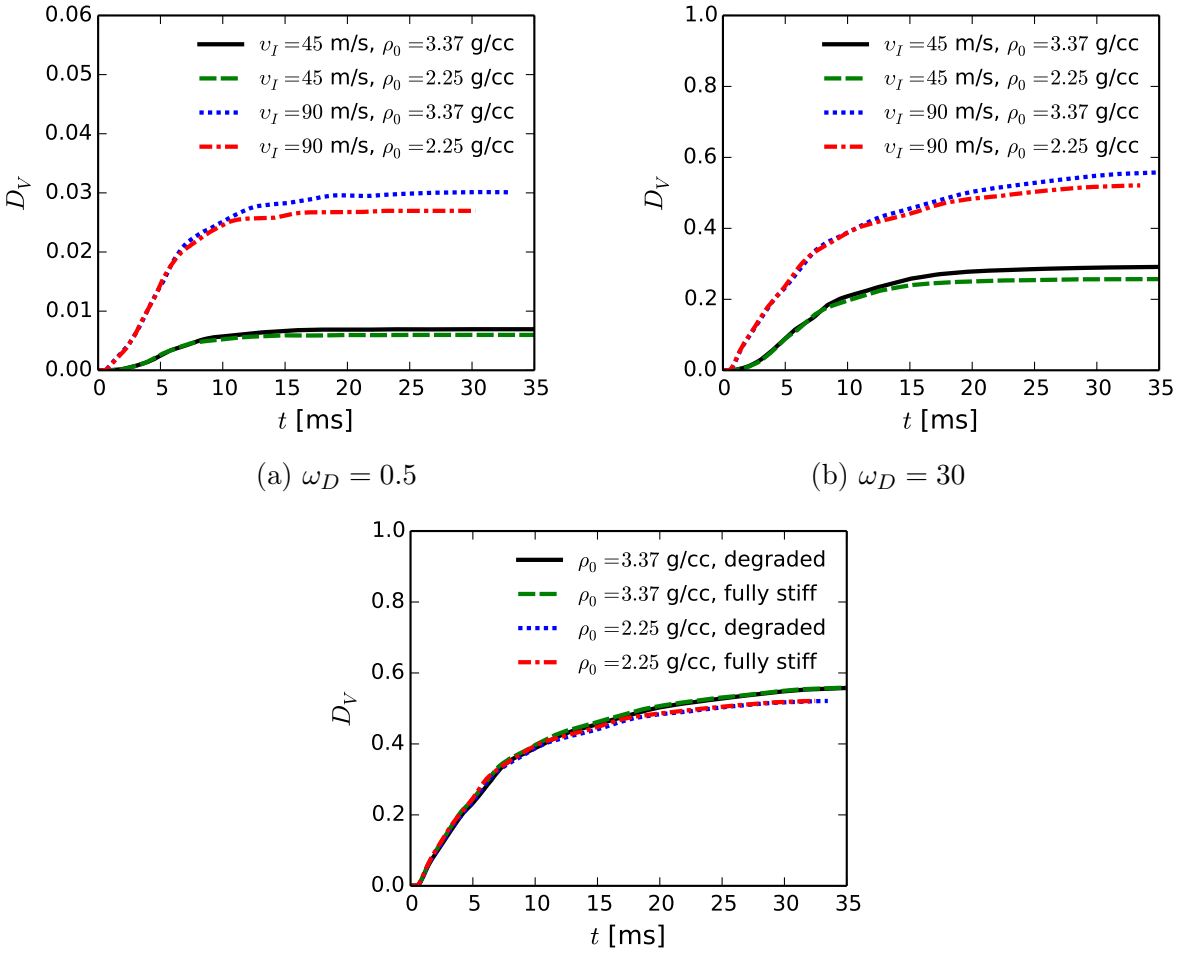

(a) $\omega_D = 0.5$

(b) $\omega_D = 30$

(c) $v_I = 90$ m/s

Fig. 15 Average damage-injury metric D_V (both lungs) versus simulation time: a) simulations 1, 2, 5, 6 ($\omega_D = 0.5$), b) simulations 3, 4, 7, 8 ($\omega_D = 30$), and c) simulations 7–10 (different stiffness options, impact velocity 90 m/s)

occurs and deflection is maximal. Denote by $u_2(t)$ and $v_2(t)$ the displacement and velocity, respectively, of the spine. Denote by d_0 the initial depth of the chest. Then the compression criterion (dimensionless) is defined as the history maximum of the normalized chest compression[46]:

$$C_{max} = \max_{t\in[0,t_f]} C(t), \qquad C(t) = \frac{u_1(t) - u_2(t)}{d_0}. \tag{94}$$

The viscous criterion (dimensions of velocity) is defined as the history maximum of the instantaneous product of $C(t)$ with the relative velocity of chest compression $V(t)$[46]:

$$\begin{aligned} VC_{max} &= \max_{t\in[0,t_f]} VC(t), \\ VC(t) &= V(t)\cdot C(t) = [v_1(t) - v_2(t)]\cdot\left[\frac{u_1(t) - u_2(t)}{d_0}\right]. \end{aligned} \tag{95}$$

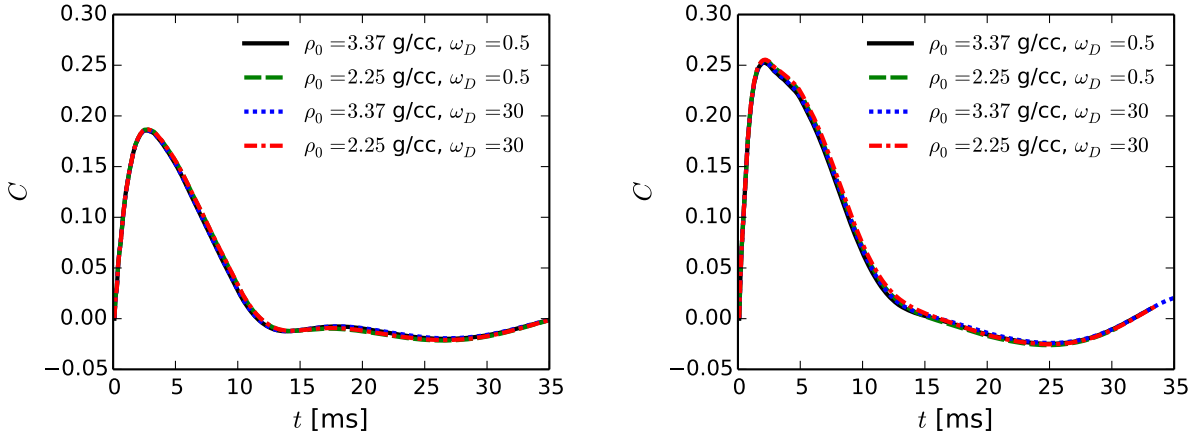

(a) $v_I = 45$ m/s (b) $v_I = 90$ m/s

Fig. 16 Compression injury criterion C versus simulation time: a) simulations 1–4 (impact velocity 45 m/s) and b) simulations 5–8 (impact velocity 90 m/s)

Evolution of $C(t)$ is reported for simulations 1 through 4 in Fig. 16a and for simulations 5 through 8 in Fig. 16b. Values of $C(t)$ are sensitive to impact velocity, with moderately larger peaks observed at 90 m/s than at 45 m/s. Differences due to different prescriptions of mass density and damage kinetics in the lung constitutive model are nearly negligible. This implies that $C(t)$ is relatively insensitive to the mechanical response of the lungs alone.

Viscous variable $VC(t)$ is reported for simulations 1 through 4 in Fig. 17a and for simulations 5 through 8 in Fig. 17b. Values of $VC(t)$ are notably sensitive to impact velocity, with significantly larger maxima witnessed at 90 m/s than at 45 m/s. Differences due to different prescriptions of mass density ρ_0 and energy rate amplification of damage ω_D are visible in some of the oscillations, but trends in results are unaffected by choices of ρ_0 or ω_D. It should be noted that calculated values of $VC(t)$ are highly dependent on the output frequency of numerical simulations since the surface velocity fluctuates tremendously near initial impact. Thus, results for VC_{max} are likely sensitive to time step size, just as they are sensitive to accelerometer resolution in physical experiments. For the present simulations, the sampling rate is 10^4/s, and data are obtained for a single critical node (with the same global node number in all simulations) rather than multiple nodes averaged over the impact region.

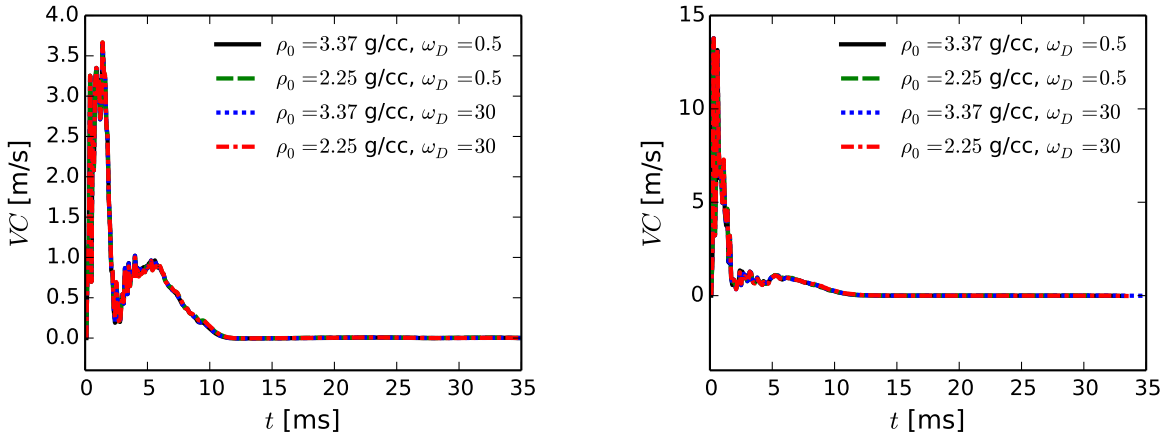

(a) $v_I = 45$ m/s (b) $v_I = 90$ m/s

Fig. 17 Viscous injury criterion VC versus simulation time: a) simulations 1–4 (impact velocity 45 m/s) and b) simulations 5–8 (impact velocity 90 m/s)

Global injury criteria defined in Eqs. 93, 94, and 95 are compared directly in Table 3. Mean values over simulation pairs at both mass densities (i.e., ρ_0 of 3.37 and 2.25 g/cc) are denoted with over-bars. At the low impact velocity of 45 m/s, no thoracic injuries were reported for live porcine experiments with the same projectile[45] at kinetic energy less than 100 J, while injuries were highly probable for the high impact velocity of 90 m/s at kinetic energy greater than 270 J.

Table 3 Likelihood of lung injury in porcine experiments[45] compared with maximum volume-averaged damage-injury parameter $\bar{D}_{V|max}$ from LS-DYNA simulations of impact of the human torso. Global injury metric $\bar{D}_V$ is mean among simulations with two different lung densities ρ_0 but the same gradient amplification factor ω_D; maximum value at $t = 30$ ms shown. Also compared are two other global thoracic injury criteria[46,47]: normalized compression criteria $\bar{C}_{max}$ and viscous criteria $\overline{VC}_{max}$, where mean values over simulations with different lung densities are calculated in the same manner.

Impact vel. v_I (m/s)	KE (J)	Exper. injury	Parameter ω_D	New metric $\bar{D}_{V\|max}$	Compression $\bar{C}_{max}$	Viscous $\overline{VC}_{max}$ (m/s)
45	73.2	No	0.5	0.00646	0.18615	3.65813
			30	0.27305	0.18625	3.65911
90	292.8	Yes	0.5	0.02854	0.25373	13.7802
			30	0.53286	0.25422	13.7802

First consider $\bar{D}_{V|max}$ in the context of Fig. 1. When the postulated lower bound $\omega_D = 0.5$ is prescribed, then the model predicts a transition from negligible to mild injury as impact velocity increases from 45 to 90 m/s, with $\bar{D}_{V|max}$ increasing from 0.006 to 0.029. However, if the upper bound $\omega_D = 30$ is prescribed instead, then the model predicts a transition from moderate to severe lung trauma as velocity increases from 45 to 90 m/s, with $\bar{D}_{V|max}$ increasing from 0.273 to 0.533. In the context of Fig. 1, damage and injury predicted at the lower impact velocity are inconsistent with experimental observations[45] that detected no visible lung trauma, albeit on porcine rather than human subjects. The present analysis suggests that $\omega_D = 0.5$ provides more physically realistic results than $\omega_D = 30$, though the former value may underpredict tissue trauma at $v_I = 90$ m/s. Additional data on human subjects (presumably and unfortunately postmortem) is needed to provide a more precise recommendation for the choice of ω_D for human lung injury. The present results do confirm, however, that bounds $0.5 \leq \omega_D \leq 30$ previously proposed[18] for animal subjects appear equally valid for human subjects.

A survey of the efficacy of the compression (C_{max}) and viscous (VC_{max}) criteria for various test subjects (e.g., human versus animal, live versus postmortem) and various loading scenarios is outside the scope of this report; some analysis in this regard is available in the references.[9,46,47] For the present loading scenario, $\bar{C}_{max}$ increases from 0.186 to 0.254 as velocity increases from 45 to 90 m/s, while $\overline{VC}_{max}$ increases from 3.66 to 13.78 m/s over the same domain. Thus, the distinction between likely injured (90 m/s) and likely noninjured (45 m/s) states is more clearly demarcated by $\overline{VC}_{max}$ than by $\bar{C}_{max}$. However, as remarked in the context of Fig. 17, the viscous

criterion is more prone to measurement errors in both simulations and experiments due to the rapidly changing surface velocity profile at the point of impact that must be resolved temporally.

Advantages of the new global lung injury metric $D_{V|max}$ are summarized as follows:

- $D_{V|max}$ is bounded on the interval [0,1], where 0 corresponds to absolutely no injury and 1 to complete tearing and loss of function of the entire organ;
- $D_{V|max}$ should be physically correlated to occurrence of specific injury mechanisms as shown in Fig. 1, though this assertion requires further validation;
- $D_{V|max}$ does not require resolution of local surface velocities or even local surface displacements;
- $D_{V|max}$ should be universally applicable to any and all loading regimes (e.g., static and dynamic, blunt impact and blast) when parameters are properly calibrated a priori, though this assertion requires further validation.

An obvious disadvantage is that $D_{V|max}$ can only be obtained through simulations; it is not physically measurable like C_{max} and VC_{max}. Hence, $D_{V|max}$ can neither be evaluated nor validated through experimental testing alone. However, C_{max} and VC_{max} interrogate dynamics of the entire torso (e.g., ribcage, spine, and multiple organs, including the lungs) and, unlike $D_{V|max}$, they do not quantify the severity of load history experienced exclusively by the lungs.

6. Conclusions

A continuum model for mechanics and local injury to lung parenchyma has been implemented in the `LS-DYNA` code as a user material subroutine. The constitutive theory, numerical algorithms, and input file syntax have been discussed. In previous work, the model was calibrated and validated versus static and dynamic animal data. Herein, parameters have been adapted, to the extent afforded by limited experimental data, for modeling the human lung.

Parametric simulations have been conducted using the ATBM 2.5 subjected to dynamic impact by a rod to the upper right chest region. Results demonstrate that

the lung constitutive model is able to predict increasing local and global lung damage with increasing impact velocity. Injury predictions are relatively insensitive to the choice of initial lung density corresponding to inspiration versus expiration. Predictions are very sensitive to the choice of kinetic parameter controlling the amplification of lung damage due to strain energy gradients or the local rate of energy deposition. Bounds on this parameter suggested in previous simulations of animal response appear equally valid for the human response. However, more experimental data is needed to enable suggestion of a precise value for this parameter.

Mesh refinement studies are recommended, since the lung mesh of the ATBM 2.5 is relatively coarse relative to that used in prior work.[18] However, the mesh size used for the lungs is comparable to that used in other regions of the ATBM 2.5, so refinement of the lung mesh alone might not alleviate any mesh dependency. Enabling of transient element deletion and/or smooth particle hydrodynamics conversion could enable simulations to accommodate higher velocity impacts without instability issues observed from severe Lagrangian mesh distortion. However, either of these options would likely prevent an accurate depiction of lung shape recovery upon unloading, after stress waves from initial impact or blast have subsided.

7. References

1. Stitzel J, Gayzik F, Hoth J, Mercier J, Gage H, Morton K, Duma S, Payne R. Development of a finite element-based injury metric for pulmonary contusion. Part I: model development and validation. Stapp Car Crash Journal. 2005;49:271–289.

2. Stuhmiller J, Chuong C, Phillips Y, Dodd K. Computer modeling of thoracic response to blast. Journal of Trauma. 1988;28:S132–S139.

3. Vlessis A, Trunkey D. Non-penetrating injury of the thorax. In: Scientific foundations of trauma. Cooper G, Dudley H, Gann D, Little R, Maynard R, editors. Butterworth Heinemann; 1997. p. 127–143.

4. Cooper G, Jonsson A. Protection against blast injury. In: Scientific foundations of trauma. Cooper G, Dudley H, Gann D, Little R, Maynard R, editors. Butterworth Heinemann; 1997. p. 258–283.

5. Clayton J, Banton R, Freed A. A nonlinear thermoelastic-viscoelastic continuum model of lung mechanics for shock wave analysis. In: Shock compression of condensed matter; Vol. 2272. Lane J, editor. AIP Conference Proceedings; 2020. p. 040001.

6. Clayton J, Freed A. A constitutive model for lung mechanics and injury applicable to static, dynamic, and shock loading. Mechanics of Soft Materials. 2020;2:3.

7. Grimal Q, Gama B, Naili S, Watzky A, Gillespie J. Finite element study of high-speed blunt impact on thorax: linear elastic considerations. International Journal of Impact Engineering. 2004;30:665–683.

8. Grimal Q, Naili S, Watzky A. A high-frequency lung injury mechanism in blunt thoracic impact. Journal of Biomechanics. 2005;38:1247–1254.

9. Shen W, Niu Y, Mattrey R, Fournier A, Corbeil J, Kono Y, Stuhmiller J. Development and validation of subject-specific finite element models for blunt trauma study. Journal of Biomechanical Engineering. 2008;130:021022.

10. Bowen I, Fletcher E, Richmond D. Estimate of man's tolerance to the direct effects of air blast. Lovelace Foundation for Medical Education and Research; 1968. Report No.: DASA 2113.

11. Cooper G, Pearce B, Sedman A, Bush I, Oakley C. Experimental evaluation of a rig to simulate the response of the thorax to blast loading. Journal of Trauma and Acute Care Surgery. 1996;40:38S–41S.

12. Rafaels K, Cameron R, Panzer M, Salzar R. Pulmonary injury risk assessment for long-duration blasts: a meta-analysis. Journal of Trauma and Acute Care Surgery. 2010;69:368–374.

13. Gibbons M, Dang X, Adkins M, Powell B, Chan P. Finite element modeling of blast lung injury in sheep. Journal of Biomechanical Engineering. 2015;137:041002.

14. Simo J. On a fully three-dimensional finite-strain viscoelastic damage model: formulation and computational aspects. Computer Methods in Applied Mechanics and Engineering. 1987;60:153–173.

15. Krajcinovic D. Damage mechanics. North-Holland; 1996.

16. Rodríguez J, Cacho F, Bea J, Doblaré M. A stochastic-structurally based three dimensional finite-strain damage model for fibrous soft tissue. Journal of the Mechanics and Physics of Solids. 2006;54:864–886.

17. Balzani D, Brinkhues S, Holzapfel G. Constitutive framework for the modeling of damage in collagenous soft tissues with application to arterial walls. Computer Methods in Applied Mechanics and Engineering. 2012;213:139–151.

18. Clayton J. Modeling lung tissue dynamics and injury under pressure and impact loading. Biomechanics and Modeling in Mechanobiology. 2020;19:2603–2626.

19. Gayzik F, Hoth JJ, Stitzel J. Finite element–based injury metrics for pulmonary contusion via concurrent model optimization. Biomechanics and Modeling in Mechanobiology. 2011;10:505–520.

20. Clayton J, Freed A. A continuum mechanical model of the lung. DEVCOM Army Research Laboratory; 2019. Report No.: ARL-TR-8859.

21. Lai-Fook S, Wilson T, Hyatt R, Rodarte J. Elastic constants of inflated lobes of dog lungs. Journal of Applied Physiology. 1976;40:508–513.

22. Hajji M, Wilson T, Lai-Fook S. Improved measurements of shear modulus and pleural membrane tension of the lung. Journal of Applied Physiology. 1979;47:175–181.

23. Jahed M, Lai-Fook S, Bhagat P, Kraman S. Propagation of stress waves in inflated sheep lungs. Journal of Applied Physiology. 1989;66:2675–2680.

24. Jahed M, Lai-Fook S, Bhagat P. Effect of vascular volume and edema on wave propagation in canine lungs. Journal of Applied Physiology. 1990;68:2171–2176.

25. Jahed M, Lai-Fook S. Stress wave velocity measured in intact pig lungs with cross-spectral analysis. Journal of Applied Physiology. 1994;76:565–571.

26. Stamenovic D. Micromechanical foundations of pulmonary elasticity. Physiological Reviews. 1990;70:1117–1134.

27. Yen R, Fung Y, Ho H, Butterman G. Speed of stress wave propagation in lung. Journal of Applied Physiology. 1986;61:701–705.

28. Fung YC. Biomechanics: motion, flow, stress, and growth. Springer; 1990.

29. Hoppin F, Lee G, Dawson S. Properties of lung parenchyma in distortion. Journal of Applied Physiology. 1975;39:742–751.

30. Lee G, Frankus A. Elasticity properties of lung parenchyma derived from experimental distortion data. Biophysical Journal. 1975;15:481–493.

31. Fung YC. Stress, deformation, and atelectasis of the lung. Circulation Research. 1975;37:481–496.

32. Fung YC, Patitucci P, Tong P. Stress and strain in the lung. ASCE Journal of Engineering Mechanics. 1978;104:201–223.

33. Vawter D, Fung YC, West J. Constitutive equation of lung tissue elasticity. Journal of Biomechanical Engineering. 1979;101:38–45.

34. Freed A, Einstein D. An implicit elastic theory for lung parenchyma. International Journal of Engineering Science. 2013;62:31–47.

35. Hughes R, May A, Widdicombe J. Stress relaxation in rabbits' lungs. Journal of Physiology. 1959;146:85–97.

36. Sanborn B, Nie X, Chen W, Weerasooriya T. High strain rate pure shear and axial compressive response of porcine lung tissue. Journal of Applied Mechanics. 2013;80:011029.

37. Butler J, Lehr J, Drazen J. Longitudinal elastic wave propagation in pulmonary parenchyma. Journal of Applied Physiology. 1987;62:1349–1355.

38. Tao Z, Fung Y. Lungs under cyclic compression and expansion. Journal of Biomechanical Engineering. 1987;109:160–162.

39. Fung YC, Yen R, Tao Z, Liu S. A hypothesis on the mechanism of trauma of lung tissue subjected to impact load. Journal of Biomechanical Engineering. 1988;110:50–56.

40. Yen R, Fung Y, Liu S. Trauma of lung due to impact load. Journal of Biomechanics. 1988;21:745–753.

41. Zeng Y, Yager D, Fung Y. Measurement of the mechanical properties of the human lung tissue. Journal of Biomechanical Engineering. 1987;109:169–174.

42. Lai-Fook S, Hyatt R. Effects of age on elastic moduli of human lung. Journal of Applied Physiology. 2000;89:163–168.

43. Saraf H, Ramesh K, Lennon A, Merkle A, Roberts J. Mechanical properties of soft human tissues under dynamic loading. Journal of Biomechanics. 2007;40:1960–1967.

44. Hallquist J. LS-DYNA user's manual R12.0. Livermore Software Technology Corporation; 2020.

45. Mathews K, Ng L. Swine test report for injury correlate development and validation. L-3 Applied Technologies; 2018. Report No.: J0511-18-725.

46. Viano D, Lau I. A viscous tolerance criterion for soft tissue injury assessment. Journal of Biomechanics. 1988;21:387–399.

47. Yuen K, Cronin D, Deng Y. Lung response and injury in side impact conditions. In: Proceedings of the 2008 International Research Council on Biomechanics of Injury (IRCOBI) Conference; p. 87–98.

48. Clayton J, Freed A. Viscoelastic-damage theory based on a QR decomposition of deformation gradient. DEVCOM Army Research Laboratory; 2019. Report No.: ARL-TR-8840.

49. Clayton J, Freed A. A constitutive framework for finite viscoelasticity and damage based on the Gram-Schmidt decomposition. Acta Mechanica. 2020;231:3319–3362.

50. Criscione J. A constitutive framework for tubular structures that enables a semi-inverse solution to extension and inflation. Journal of Elasticity. 2004;77:57–81.

51. Holzapfel G, Simo J. A new viscoelastic constitutive model for continuous media at finite thermomechanical changes. International Journal of Solids and Structures. 1996;33:3019–3034.

52. Holzapfel G. On large strain viscoelasticity: continuum formulation and finite element applications to elastomeric structures. International Journal for Numerical Methods in Engineering. 1996;39:3903–3926.

53. Rice D. Sound speed in pulmonary parenchyma. Journal of Applied Physiology. 1983;54:304–308.

54. Tsokos M, Paulsen F, Petri S, Madea B, Puschel K, Turk E. Histologic, immunohistochemical, and ultrastructural findings in human blast lung injury. American Journal of Respiratory and Critical Care Medicine. 2003;168:549–555.

55. Freed A, Graverend J, Rajagopal K. A decomposition of Laplace stretch with applications in inelasticity. Acta Mechanica. 2019;230:3423–3429.

56. Freed A. A note on stress/strain conjugate pairs: Explicit and implicit theories of thermoelasticity for anisotropic materials. International Journal of Engineering Science. 2017;120:155–171.

57. Freed A, Zamani S. On the use of convected coordinate systems in the mechanics of continuous media derived from a QR factorization of F. International Journal of Engineering Science. 2018;127:145–161.

58. Freed A, Zamani S. Elastic Kelvin-Poisson-Poynting solids described through scalar conjugate stress/strain pairs derived from a QR factorization of F. Journal of the Mechanics and Physics of Solids. 2019;129:278–293.

59. Srinivasa A. On the use of the upper triangular (or QR) decomposition for developing constitutive equations for Green-elastic materials. International Journal of Engineering Science. 2012;60:1–12.

60. Clayton J. Compatibility conditions from a Gram-Schmidt decomposition of deformation gradient in two dimensions. Mechanics Research Communications. 2020;104:103498.

61. Paul S, Freed A. A constitutive framework for finite viscoelasticity and damage based on the Gram-Schmidt decomposition. Acta Mechanica. 2020;231:3289-3304.

62. Clayton J. On anholonomic deformation, geometry, and differentiation. Mathematics and Mechanics of Solids. 2012;17:702–735.

63. Clayton J. Differential geometry and kinematics of continua. World Scientific; 2014.

64. McLellan A. The classical thermodynamics of deformable materials. Cambridge University Press; 1980.

65. Freed A, Paul S, Clayton J. Coordinate indexing: on the use of Eulerian and Lagrangian Laplace stretches. Applications in Engineering Science. 2021;5:100029.

66. Clayton J. Nonlinear mechanics of crystals. Springer; 2011.

67. Clayton J. Nonlinear elastic and inelastic models for shock compression of crystalline solids. Springer; 2019.

68. Vawter D. A finite element model for macroscopic deformation of the lung. Journal of Biomechanical Engineering. 1980;102:1–7.

69. Hoppin F, Stothert J, Greaves I, Lai YL, Hildebrandt J. Lung recoil: elastic and rheological properties. In: Handbook of physiology. The respiratory system. Mechanics of breathing. American Physiological Society; 1986. p. 195–216.

70. Davison L. Fundamentals of shock wave propagation in solids. Springer; 2008.

71. Fung YC. Elasticity of soft tissues in simple elongation. American Journal of Physiology. 1967;213:1532–1544.

72. Fung YC. Biomechanics: mechanical properties of living tissues. Second ed. Springer; 1993.

73. Inoue H, Inoue C, Hildebrandt J. Temperature effects on lung mechanics in air-and liquid-filled rabbit lungs. Journal of Applied Physiology. 1982;53:567–575.

74. Clayton J, Knap J. A geometrically nonlinear phase field theory of brittle fracture. International Journal of Fracture. 2014;189:139–148.

75. Clayton J, Knap J. Phase field modeling of coupled fracture and twinning in single crystals and polycrystals. Computer Methods in Applied Mechanics and Engineering. 2016;312:447–467.

76. Clayton J. Finsler geometry of nonlinear elastic solids with internal structure. Journal of Geometry and Physics. 2017;112:118–146.

77. Clayton J. Generalized finsler geometric continuum physics with applications in fracture and phase transformations. Zeitschrift fur Angewandte Mathematik und Physik (ZAMP). 2017;68:9.

78. Grimal Q, Watzky A, Naili S. A one-dimensional model for the propagation of transient pressure waves through the lung. Journal of Biomechanics. 2002;35:1081–1089.

79. Hallquist J. LS-DYNA theory manual. Livermore Software Technology Corporation; 2006.

80. D'yachenko A, Manyuhina O. Modeling of weak blast wave propagation in the lung. Journal of Biomechanics. 2006;39:2113–2122.

81. Ochs M, Nyengaard J, Jung A, Knudsen L, Voigt M, Wahlers T, Richter J, Gundersen H. The number of alveoli in the human lung. American Journal of Respiratory and Critical Care Medicine. 2004;169:120–124.

82. Lai-Fook S. The elastic constants of lung parenchyma: the effect of pressure–volume hysteresis on the behavior of blood vessels. Journal of Biomechanics. 1979;12:757–764.

83. Wahl P, Schreyer N, Yersin B. Injury pattern of the flash-ball®, a less-lethal weapon used for law enforcement: report of two cases and review of the literature. The Journal of Emergency Medicine. 2006;31:325–330.

Appendix. Input File Syntax for LS–DYNA

The constitutive model of Section 2 is implemented, with numerical algorithms of Section 3, as a user material subroutine in the LS−DYNA software, version R12.0 (2020). Recommended units (i.e., mass-length-time-force-stress-temperature, not all independent) are **kg-m-sec-N-Pa-K**. Notation for constitutive parameters in what follows corresponds to nomenclature in Table 1 of Section 4. The model has only been verified for ⋆ELEMENT_SOLID elements (e.g., shell elements are not supported).

Input is provided through LS−DYNA keyword syntax with the following cards:

MAT_050
⋆MAT_USER_DEFINED_MATERIAL_MODELS

CARD 1

- MID: material identification—unique 8-digit number.
- RO: initial mass density ρ_0; must match entry 8 of Card 3.
- MT: material number for user-defined subroutine call (fixed).
- LMC: length of material constant array (total no. of entries of Cards 3 and 4).
- NHV: number of user history variables in hsv vector (fixed; see Section 3).
- IORTHO: material is not orthotropic (fixed).
- IBULK: card 3 entry no. of bulk modulus for time step calculation (fixed).
- IG: card 3 entry no. of shear modulus for time step calculation (fixed).

CARD 2

- IVECT: non-vectorized material model (fixed).
- IFAIL: failure flag not implemented (fixed).
- ITHERM: temperatures implemented (fixed).
- IHYPER: deformation gradient in positions NHV+1 to NHV+9 of hsv (fixed).
- IEOS: separate equation of state not used (fixed).

CARD 3

- `BD`: dynamic closed-cell isentropic bulk modulus $\bar{B}_d^\eta = \bar{B}_0^\eta + \beta_1 B_0^T$.
- `GD`: dynamic shear modulus $G_d = G_0 \cdot (1 + \beta_3)$.
- `C1`: exponential bulk stiffening c_1.
- `C2`: exponential squeeze stiffening c_2.
- `C3`: exponential shear stiffening c_3.
- `GP`: ambient pressure derivative of shear modulus $G_0' = \mu_0'$.
- `K0`: initial surface tension K_0.
- `RO`: initial mass density ρ_0; must match entry 2 of Card 1.

CARD 4

- `BT`: static isothermal bulk modulus $B_0^T \approx B_0^\eta$.
- `BETA1`: viscoelastic stiffening $\beta_1 = \mu_1 / B_0^T = 6 G_0 \beta_2 / B_0^T = G_0 \beta_3 / B_0^T$.
- `CV`: specific heat per unit volume at constant volume c_0.
- `GRUN`: Grüneisen parameter g_0.
- `Z0`: local damage-injury initiation threshold Z_0 (must be nonzero); if $Z_0 < 0$, fully intact stiffness option of Section 2.9 invoked with $Z_0 \to |Z_0|$.
- `ALPHD`: damage-injury kinetic coefficient α_D.
- `OMEGD`: damage-injury kinetic rate amplification ω_D.
- `L`: mean alveolar diameter l.

Alteration of values denoted as "fixed" will likely result in code execution failure. Nonphysical prescriptions of conventionally positive quantities (e.g., zero-valued or negative stiffness moduli) similarly will cause code execution failure.

Card 1	1	2	3	4	5	6	7	8
Variable	MID	RO	MT	LMC	NHV	IORTHO	IBULK	IG
Required	user-prescribed	matches Card 3	**50**	**16**	**6**	**0**	**1**	**2**
Type	A8	F	I	I	I	I	I	I

Card 2	1	2	3	4	5	6	7	8
Variable	IVECT	IFAIL	ITHERM	IHYPER	IEOS			
Required	**0**	**0**	**1**	**1**	**0**			
Type	I	I	I	I	I			

Card 3	1	2	3	4	5	6	7	8
Variable [units]	BD [Pa]	GD [Pa]	C1 [none]	C2 [none]	C3 [none]	GP [none]	K0 [Pa]	RO [kg/m^3]
Suggested	2.18E+05	7.5E+03	3.0	10.0	1.0	−0.70	600.0	337.0
Type	F	F	F	F	F	F	F	F

Card 4	9	10	11	12	13	14	15	16
Variable [units]	BT [Pa]	BETA1 [none]	CV [Pa/K]	GRUN [none]	Z0 [none]	ALPHD [none]	OMEGD [none]	L [m]
Suggested	7.5E+03	0.60	7.41E+05	4.91E-04	± 0.64	0.0167	0.5-30.0	1.8E-04
Type	F	F	F	F	F	F	F	F

1 (PDF) DEFENSE TECHNICAL INFORMATION CTR DTIC OCA

1 (PDF) DEVCOM ARL FCDD RLD DCI TECH LIB

2 (PDF) MEDCOM USAMRMC R GUPTA C STEELE

1 (PDF) DEVCOM DAC FCDD DAD OP N EBERIUS

1 (PDF) US ARMY ITC-CANADA D SCOOLER

1 (PDF) CARLETON UNIV O PETEL

1 (PDF) TEXAS A&M UNIV A FREED

1 (PDF) UNIV COLORADO R REGUEIRO

ABERDEEN PROVING GROUND

36 (PDF) DEVCOM ARL
FCDD RLC HC
J KNAP
FCDD RLW
S KARNA
A RAWLETT
S SCHOENFELD
J ZABINSKI
FCDD RLW MB
G GAZONAS
FCDD RLW PB
R BANTON
T BAUMER
A BROWN
A DAGRO
A EIDESMORE
A GOERTZ
C HOPPEL
M KLEINBERGER
K RAFAELS
S SATAPATHY
M SCHEIDLER
S WOZNIAK
FCDD RLW PC
R BECKER
J BERRY
D CASEM
J CAZAMIAS
J CLAYTON
M FERMEN-COKER
A FREED
M GREENFIELD
R LEAVY
J LLOYD
C MEREDITH
R REGUEIRO
S SEGLETES
L SHANNAHAN
A TONGE
S TURNAGE
C WILLIAMS
FCDD RLW PE
P GILLICH